

The Tully-Fisher Relation as a Measure of Luminosity Evolution: A Low Redshift Baseline for Evolving Galaxies¹

Elizabeth J. Barton

Herzberg Institute of Astrophysics, National Research Council of Canada

and

Margaret J. Geller

Harvard-Smithsonian Center for Astrophysics

and

Benjamin C. Bromley

Department of Physics, University of Utah

and

Liese van Zee

Herzberg Institute of Astrophysics, National Research Council of Canada

and

Scott J. Kenyon

Harvard-Smithsonian Center for Astrophysics

ABSTRACT

We use optical rotation curves to investigate the *R*-band Tully-Fisher properties of a sample of 90 spiral galaxies in close pairs, covering a range of luminosities, morphological types, and degrees of tidal distortion. The galaxies follow the Tully-Fisher relation remarkably well, with the exception of eight distinct $\sim 3\sigma$ outliers. Although most of the outliers show signs of recent star formation, gasdynamical effects are probably the dominant cause of their anomalous Tully-Fisher properties. Four outliers with small emission line widths have very centrally concentrated line emission and truncated rotation curves; the central emission indicates recent gas infall after a close galaxy-galaxy pass. These four galaxies may be local counterparts to compact, blue galaxies at intermediate redshift.

The remaining galaxies have a negligible offset from the reference Tully-Fisher relation, but a shallower slope (2.6 σ significance) and a 25% larger scatter. We argue

¹ Some observations reported in this paper were obtained at the Multiple Mirror Telescope Observatory, a facility operated jointly by the University of Arizona and the Smithsonian Institution.

that triggered star formation is a significant contributor to the slope difference. We characterize the non-outlier sample with measures of distortion and star formation to search for third parameter dependence in the residuals of the TF relation. Severe kinematic distortion is the only significant predictor of TF residuals; this distortion is not, however, responsible for the slope difference from the reference distribution.

Because the outliers are easily removed by sigma clipping, we conclude that even in the presence of some tidal distortion, detection of moderate ($\gtrsim 0.5$ magnitudes in rest-frame R) luminosity evolution should be possible with high-redshift samples the size of this 90-galaxy study. The slope of the TF relation, although difficult to measure, is as fundamental for quantifying luminosity evolution as the zero-point offset.

Subject headings: galaxies: evolution — galaxies: fundamental parameters — galaxies: interactions — galaxies: kinematics and dynamics — galaxies: spirals

1. Introduction

Tully-Fisher (1977; TF hereafter) luminosity-linewidth studies frequently exploit the TF relation as a secondary distance indicator. As the fundamental scaling relation for spiral galaxies, the TF relation also provides constraints on galaxy formation; it is deeply connected to the processes by which disk galaxies form (e.g., Cole et al. 1994; Eisenstein & Loeb 1996; Navarro & Steinmetz 2000; Mo & Mao 2000). By allowing comparisons of galaxies at high z to *physically similar* systems at the present day, the TF relation for spirals and the fundamental plane for spheroid-dominated systems provide crucial anchors for measuring luminosity evolution directly.

Both the TF and the fundamental plane relations are indispensable for establishing a complete picture of galaxy evolution. Kinematic estimates are frequently necessary for ascertaining the masses of galaxies. For example, the faint, compact, blue galaxies may be small, starbursting galaxies that will eventually fade or larger galaxies with only moderate amounts of star formation (Koo et al. 1994, 1995; Kobulnicky & Zaritsky 1999). Only kinematic linewidths that truly reflect the masses of these galaxies would resolve the degeneracy. To date, TF studies of galaxies at large redshift with resolved rotation curves contain few galaxies and yield discrepant results; Simard & Pritchett (1998) find an offset of 1.5 – 2 magnitudes, while Vogt et al. (1996; 1997) find evidence for only a moderate offset ($\lesssim 0.4$ magnitudes in B). With the advent of 8-m class telescopes, the size of these studies will increase and an understanding of the underlying physics will be crucial. Until now, the primary goal of large TF studies has been construction of the tightest relation possible for use as a distance indicator; thus most local TF studies are limited in morphology, excluding galaxies with signs of interaction and/or tidal distortion (e.g., Rubin et al. 1985; Pierce & Tully 1992; Willick et al. 1995; Willick et al. 1996; Bureau, Mould, & Staveley-Smith 1996; Giovanelli et al. 1997a; Giovanelli et al. 1997b; Giovanelli et al. 1997c; Courteau 1997; Dale et al. 1997; Haynes et al. 1999a; Haynes et al. 1999b; Dale et al. 1999; Tully & Pierce 2000).

With application to high redshift in mind, we explore the effects of loosening the morphological and environmental constraints that the largest studies apply. Pruning of high- z TF samples is more difficult because interactions are more frequent and the signatures of interaction are not so readily observable. Low surface brightness companions, minor merger remnants embedded in larger galaxies, and faint tidal features can fall below the detection limits. Seeing effects obscure both morphological and kinematic distortion. The desired measurement of luminosity evolution may become confused by the effects of tidal distortion on the measurements of the galaxy parameters. Thus, high-redshift studies must rely on knowledge of the statistical effects of interactions gleaned from low-redshift studies.

The TF relation has not yet been extensively studied as a means of detecting evolution. We consider the slope of the TF relation and the outliers to the distribution, in addition to the zero-point offset, as fundamental tools for characterizing luminosity evolution and morphological evolution.

We explore the TF properties of 90 galaxies in the Barton, Geller, & Kenyon (2000a; BGK hereafter) sample of galaxies in close pairs and n-tuples. Because BGK find the distinct signature of increased star formation due to interactions, the BGK sample provides an ideal testing ground for the use of the TF relation to detect moderate luminosity evolution. We lay the groundwork for future TF studies of high-redshift galaxies by: (1) quantifying the effects of moderate distortion on the, intercept, slope and outliers of the TF relation, and (2) setting limits on the ability of pre- or non-merger interaction to initiate luminosity evolution off the TF relation at the current epoch. Thus, our study complements searches for TF deviations in low-mass or low-surface brightness galaxies (Sprayberry et al. 1995; Courteau & Rix 1999; O’Neil et al. 2000; McGaugh et al. 2000), extreme late-type galaxies (Matthews, van Driel, & Gallagher 1998), S0s (Neinstein et al. 1999), and asymmetric galaxies (Zaritsky & Rix 1997), and for non-linearity in the relation (Mould, Han, & Bothun 1989).

In Sec. 2, we describe the sample and the data reduction and analysis procedures. We discuss the TF properties of paired galaxies and identify the outliers to the TF relation in Sec. 3. In Sec. 4, we explore the expected effects of tidal and kinematic distortion and luminosity evolution; we interpret the outliers in light of these expectations and identify 4 outliers with similar systems at intermediate redshift, the compact, blue galaxies with narrow emission lines. In Sec. 5, we develop empirical measures of distortion and luminosity evolution; we test these measures for correlations with the TF residuals, and we examine causes of the differences between the pair TF distribution and the reference TF distribution. We discuss the implications of our results for high-redshift evolution studies in Sec. 6 and we conclude in Sec. 7.

2. The Observations

In this section, we describe the sample and the data reduction and analysis procedures.

2.1. The Sample

We draw the TF sample from the set of all 786 galaxies in pairs and n-tuples in the original CfA2 redshift survey with $\Delta D \leq 50 \text{ h}^{-1} \text{ kpc}$, $\Delta V \leq 1000 \text{ km/s}$ and $v \geq 2300 \text{ km/s}$, where ΔV is the pair (or n-tuple neighbor) velocity separation, and $v = cz$ is the apparent recession velocity. This TF sample is a subset of the BGK sample; the full sample is 70% complete with respect to all known galaxies in pairs in their updated CfA2 redshift survey region (Falco et al 1999).

The sample spans a luminosity range typical of many TF studies ($-21.74 \leq M_B \leq -17.68$, corrected for extinction and assuming $H_0 = 70 \text{ km s}^{-1} \text{ Mpc}^{-1}$). The nominal magnitude limit of the CfA2 redshift survey, $m_B \approx m_{Zw} = 15.5$, corresponds to an absolute magnitude $M_B \sim -21.0$ at the largest redshift in the sample ($z = 0.0478$).

In spite of the $m_{Zw} = 15.5$ cutoff, the pair sample contains numerous galaxies with $m_B > 15.5$. These systems were often recorded in the CGCG (Zwicky 1961-1968) with the Zwicky magnitude of the whole system, rather than with separate magnitudes for each of the galaxies. Eighteen (of 90) galaxies (20%) in the TF sample have $m_B > 15.5$, where m_B is the total B magnitude (see Sec. 2.5). The sample is incomplete with respect to these galaxies; we use the Willick (1994) technique to model the resulting biases in Sec. 3.

We have different data for different subsamples of the pairs. In this paper, we concentrate on the TF properties of the 90 galaxies for which we have optical rotation curves, additional nuclear spectra (for all but one), and B and R images. We eliminate galaxies with $i < 40^\circ$ and with slit misalignment correction factors $\geq 18.3\%$ [larger than the error in velocity width implied by the 1σ scatter from the Courteau (1997) TF distribution, 0.46 magnitudes]. Sec. 2.4 describes the corrections for inclination and misalignment.

We selected systems for rotation curve measurement based on the availability of $\text{H}\alpha$ emission for the kinematic measurements; this subsample favors $\text{H}\alpha$ -emitting galaxies and spirals with inclinations $\gtrsim 50^\circ$ (see BGK). We exclude some of the most distorted galaxies in pairs, typically if they no longer appear to have a disk. Fig. 1 shows a modified version of Fig. 2 from BGK. In BGK, the figure shows the primary evidence that star formation is triggered by a close pass — the $\text{EW}(\text{H}\alpha)$ of BGK galaxies correlates with pair separation on the sky, ΔD . Here, starred points show the placement of the 89 TF target galaxies with nuclear spectra. For the galaxies without significant nuclear $\text{H}\alpha$ emission, we use the disk $\text{H}\alpha$ emission to measure the rotation curves.

Selection biases play an important role in any TF study. However, apart from our deliberate selection of galaxies in (resolved) pairs or tight systems, most TF studies share our most important biases: (1) we favor systems with substantial line emission, necessary to measure optical rotation curves, (2) our magnitude-limited sample includes intrinsically faint galaxies only if they are nearby, and (3) we include only disk galaxies. Therefore, the effects of interactions should explain any significant differences between the TF properties of our sample and reference samples. Sec. 2.4 explores the selection of the comparison samples.

2.2. The Emission Line Rotation Curves

We observed galaxies in the dynamical sample with the Blue Channel Spectrograph at the Multiple Mirror Telescope on Mt. Hopkins between November 1996 and February 1998. For the majority of the galaxies, we used a 1" slit, with a 1200 lines/mm grating centered at \sim 6500 Å. The spectra cover roughly the wavelength range 5800 – 7200 Å. We usually expose for 2×15 minutes per galaxy.

To reduce the data, we employ cross-correlation, which makes simultaneous use of the major emission lines: [NII] (λ 6548 and λ 6583), [SII] (λ 6716 and λ 6730), and H α (see Barton et al. 2000c). We construct synthetic cross-correlation templates based on median linewidths and relative heights throughout each observing run. The technique is straightforward to implement and yields well-defined errors that enlarge in the presence of multiple velocity components or low signal-to-noise data.

2.3. The Photometry

We observed the galaxies at the FLWO 48" telescope on Mt. Hopkins through either Johnson-Cousins or Harris *B* and *R* filters, for total exposure times of 15 minutes (usually spread over 3 images) and 5 minutes (with 1 or 2 images), respectively. Almost all of the pairs and n-tuples fit entirely on the Loral 2048 \times 2048 CCD, which covers an $\sim 11' \times 11'$ field, with $\sim 0''.63$ per pixel when binned by 2. The observations spanned several observing runs between November 1996 and March 1999.

We bias subtract, flatfield, and cosmetically correct the data using standard procedures and the CCDRED tasks in IRAF.

We sky-subtract and measure magnitudes and surface brightness profiles using the GALPHOT package, originally written for surface photometry by Freudling (1993), and updated by N. Grogan (see Grogan & Geller 1999) to overlay fitted *B*-band isophotes onto *R*-band images. On both the *B* and *R* images, we measure the sky level in boxes placed around the galaxy or pair. We blank out stars on or around the galaxies using the **imedit** task in the IMAGES package.

With GALPHOT tasks, which make use of several tasks in the ISOPHOTE package, we fit the remaining (good) data on the *B* images with isophotal ellipses. When the signal-to-noise ratio fades in the outskirts of each galaxy, we fix the center, position angle and ellipticity based on the inner isophotal ellipses. Assuming symmetry within the isophotal ellipses (sometimes not a well-justified assumption) the **sphot** driver task in GALPHOT constructs a model for the “blanked-out” data, and “cleans” the image with this model. On rare occasions, when the galaxies are very far from axisymmetric, we use the **imedit** task to interpolate locally over stars. In either case, **sphot** uses the cleaned image for the final photometry.

sphot overlays the B ellipses onto the R image to obtain a directly comparable R -band surface brightness profile. It constructs a new R model based on the good available data, and derives a set of isophotal magnitudes from the cleaned R image (see Grogin & Geller 1999 for details).

Our study focuses on interacting galaxies; therefore, several systems are either highly disturbed or contain overlapping galaxies. Our methods of dealing with these systems vary from system to system. In general, we fit ellipses where possible, sometimes smoothing the image for fitting purposes, but we fix the ellipse parameters if necessary. When galaxies overlap, but the individual galaxies are roughly elliptically symmetric, we derive magnitudes iteratively. We blank out one of the galaxies, fit the second galaxy, subtract the model for the second galaxy, and fit the first again. For most systems, this procedure is sufficient, but in some cases we continue to iterate until the model subtraction appears adequate. In the worst few cases, when galaxies overlap and are not symmetric, we arbitrarily divide the flux between the galaxies.

We calibrate the images using Landolt (1992) standard fields. When possible, we calibrate long exposures directly. However, we observed most of the systems on mildly to moderately cloudy nights. We calibrate these data using short exposures on photometric nights. We calculate photometric offsets with the available stars on the frame.

Photometric errors vary from system to system. The most important factors are: (1) the calibration procedure, and (2) galaxy overlap. A small number of repeat observations (on non-photometric nights, calibrated with the same short photometric exposure) suggest that the photometric differences between images average ~ 0.03 magnitudes and are $\lesssim 0.05$ magnitudes (with a few outliers). The rms scatter of standard stars on nominally photometric nights (or half-nights) satisfies $\sigma \lesssim 0.023$ magnitudes. The rms scatter in the calibration from shorter exposures falls in the range of $0.015 - 0.07$, leading to errors in the offsets (sigmas of the mean) of $0.002 - 0.015$ magnitudes. The additional errors in the magnitudes due to significant overlap of paired galaxies can sometimes be $\gtrsim 0.1$ magnitudes. Finally, bright stars nearby on the frame can add errors due to poor background subtraction. Sec. 4.3 explores the effects of some of these errors.

2.4. The Reference Tully-Fisher Distributions

We compare our pair sample primarily to the TF study of Courteau (1997; C97 hereafter), because he derives velocity measures from optical rotation curves of comparable quality and his sample is drawn from regions of quiet Hubble flow, outside the cores of rich clusters. However, the C97 study uses the Gunn r filter; our photometry is in B and R . Therefore, we also consider the Pierce & Tully (1992; PT92 hereafter) and Tully & Pierce (2000; TP00 hereafter) radio B and R relations; many high- z TF studies use the PT92 B relation as a reference distribution.

The sample selection criteria differed for these three samples. Unlike our sample which

includes all types of disk galaxies, the C97 sample consists of unbarred Sb and Sc galaxies in the UGC (see Courteau 1996). Courteau eliminates “all peculiar and interacting galaxies”; he restricts the sample to inclinations between 55° and 75° , and $m_{\text{zw}} \leq 15.5$ as for our sample. The sample TP92 use for zero-point fitting includes 15 galaxies in the Local Group, the Sculptor group, and the M81 group, with “normal” morphology and low extinction corrections; 6 of these have reliable independent distance measurements. They restrict the sample to inclinations $\geq 40^\circ$. TP92 include 32 galaxies from the Ursa Major cluster to derive the slope of the TF relation. Finally, TP00 measure a TF slope from a magnitude-limited set of galaxies in clusters (both barred and unbarred); TP00 derive the zero point from a restricted set of 24 calibrators. In summary, our selection criteria differ from the criteria applied by C97, PT92, and TP00, but the major difference between our sample and the C97, TP92, and TP00 samples is that we include only galaxies in close pairs.

2.5. The Tully-Fisher Parameters

In this section, we discuss measurements of the TF parameters. Our goal is to minimize systematic differences in measurement techniques between our pair sample and other TF studies. Therefore, we emulate as many of these previously published techniques as possible. We discuss the C97 parameters first. The adjustments for comparison to the PT92 and TP00 relations follow. Table 1 lists the set of parameters we measure.

Like C97, we use ellipse fits to derive corrected total magnitudes. However, instead of fitting ellipses in r , we fit ellipses in B and then transfer them to R . We correct the magnitudes from Gunn r to the Johnson-Cousins system with $r - R = 0.354$ (Jørgensen 1994). Following C97 we correct the $\mu_r = 26$ isophotal magnitudes to total magnitudes; in some cases, tidal distortion in the outer isophotes introduces uncertainties in the extrapolation. We compute internal reddening following C97 and Galactic reddening from n_{HI} , the HI column density. We compute the absolute magnitudes assuming the C97 value $H_0 = 70 \text{ km s}^{-1} \text{ Mpc}^{-1}$. The magnitude errors we compute include: (1) \sqrt{N} photon noise (from the signal and the sky), (2) a sky subtraction error of 15% of the sky σ , (3) 0.03 magnitudes added in quadrature for photometric calibration (0.05 if we calibrate off a shorter exposure), (4) 0.1 magnitudes added in quadrature for each case of galaxy overlap or significant interference from stars on the frame, (5) an error in Galactic extinction of 20% of the correction, (6) an error in internal extinction based on the error in inclination and, (7) a distance error from a peculiar velocity assuming $\sigma_v = \Delta V/2$, where σ_v is the error in the systemic (galactocentric) velocity of the galaxy and ΔV is the velocity separation between the galaxy and its neighbor (or the member of its n -tuple with the smallest velocity separation). The R -band total errors range from 0.07 to 0.52 magnitudes.

We usually compute the ellipticity, ϵ , and the position angle, from the $\mu_R = 24.5$ isophotal ellipse. In 21 cases, because of distortion, we use isophotal ellipses closer to the center of the galaxy, with $21.5 \leq \mu_R \leq 24.0$. We estimate the error, σ_ϵ , from the fluctuation in ϵ as a function

of radius within 5'' of the fiducial isophote, or at the faintest isophote we fit. In cases of distortion where we do not fit the ellipses directly, we assume an error of 0.1 in ellipticity. We use C97 Equation 6 to convert from ϵ to an inclination, i ; C97 assume an intrinsic flattening ratio of $q_0 = 0.18$.

We compute the disk scale length, R_{disk} , by fitting the surface brightness of the outer parts of the galaxy disk with an exponential profile. In most cases, we follow Courteau's (1996) prescription, computing r_{26} , the radius of the $\mu_r = 26$ isophotal ellipse, and fitting an exponential disk between $0.5r_{26}$ and $0.9r_{26}$ (again assuming $r - R = 0.354$). In 4 cases, where distortions affect the outer disks substantially, we fit at smaller radii. In Sec. 4.3, we consider the reduced χ^2 of the fit, χ^2_{phot} , as a measure of our ability to compute and interpret R_{disk} parameters accurately.

To measure velocity widths, we follow C97 and fit each rotation curve with an empirical fitting function (see C97, Equation. 2). In distorted cases, we fit the function anyway; we discuss the effects of this “naive” approach extensively in Secs. 4 and 5. We measure $V_{2.2}$, the velocity width of the galaxy, by evaluating the difference in the rotation curve model velocities at radii of $2.15R_{\text{disk}}$ on either side of the galaxy.

Slit misalignment from the major axis is an issue for some galaxies; for an optically and geometrically thin disk, misalignment reduces the measured velocity width by a factor:

$$f_{\text{align}} = \left[1 + \left(\frac{\tan m}{\cos i} \right)^2 \right]^{-1/2}, \quad (1)$$

where m is the angle of misalignment between the slit and the photometric major axis in the plane of the sky and i is the inclination. We compute the corrected velocity, V_c , using C97 Eqn. 4 plus the misalignment correction:

$$V_c = \frac{V_{2.2}}{(1+z) \sin(i) f_{\text{align}}}, \quad (2)$$

where z is the (galactocentric) redshift of the galaxy. Our errors include terms for all of these factors, assuming the inclination errors described above, $\sigma_z = 0.00017$, $\sigma_{V_{2.2}} = 8 \text{ km s}^{-1}$ (see C97), and $\sigma_m = 2^\circ$. Here, σ_z , $\sigma_{V_{2.2}}$, and σ_m are the errors in redshift, $V_{2.2}$, and major axis misalignment angle, respectively.

PT92 and TP00 apply somewhat different prescriptions for their parameter measurements. When we compare with their TF relations, we adjust our Hubble constant and our measurements of inclination angle and internal extinction (and the parameters these depend on) to match the prescriptions in PT92 (see also Tully & Fouqué 1985) and TP00. Therefore, we assign several magnitudes, computed according to the different distributions, to each galaxy in our sample.

The biggest systematics, however, probably arise in the conversions from optical linewidths to radio 20%-peak widths, W_{20} . C97 provides a conversion from $V_{2.2}$ to 50% widths, W_{50} . We convert from W_{50} to W_{20} following Haynes et al. (1999b), and add the turbulence correction of Tully & Fouqué (1985), to arrive at the measure of V_c which we use when comparing our sample with the PT92 and TP00 TF relations.

3. The Tully-Fisher Relation

In Fig. 2 we plot the R -band TF relation. We plot the corrected R magnitude, M_R , as a function of $\eta = \log V_c - 2.5$. The solid line is Courteau’s TF relation (shifted according to the relation $r - R = 0.354$ from Jørgensen 1994); the dotted lines illustrate his 0.46-magnitude scatter. We show the TP00 (cluster/group galaxy) relations in Fig. 3.

Fig. 2 shows that the galaxies lie on a TF relation similar to the (optical) relation of “field” galaxies, with only a few exceptions near the faint end. As a first measure of the agreement with the reference TF relations, we list the offset and scatter in Table 2. We compute these measures with a prescription similar to that of Vogt et al. (1997), by fitting for the Tully-Fisher offset while keeping the slope fixed to the slope of the reference distribution. We quote the sigma-of-the-mean as the error in the offset, and the rms value of the difference between the measured magnitude and the expected magnitude, offset by Δ_{TF} , as the scatter. We detect no net offset from the C97 TF distribution with this simple measure; the scatter increases substantially, however, from the C97 value of 0.46 magnitudes to 1.0 magnitude here.

The radio TF relations present a somewhat different picture. We find substantial deviations, Δ_{TF} , from the TP00 distribution (0.46 – 0.50 magnitudes) and even larger deviations from the PT92 distribution (0.75 – 0.87 magnitudes). In principle, we eliminate simple systematic errors which originate from different measurement techniques by altering our prescriptions for computing the TF parameters. Barring errors in the C97 radio to optical conversion, the different offsets between our sample and the reference distributions probably reflect *real* discrepancies among the reference distributions. Wherever the errors lie, the discrepancies between the C97, PT92, and TP00 TF distributions have important implications for any study which compares the TF properties of a set of galaxies to a TF reference distribution. In particular, the discrepancies may be responsible for the 0.4-magnitude offset for high- z galaxies from Vogt et al. (1997), who compare to the PT92 B -band distribution. (Vogt et al. are careful to note that their measured offset is an upper limit.)

In the following three sections, we develop a more rigorous test for true departures from the C97 reference TF distribution. In Sec. 3.1 we apply the Willick (1994) correction for luminosity bias to determine the TF slope and offset for each sample. We describe a Monte Carlo test in Sec. 3.2 which we use to measure the significance of offsets. In Sec. 3.3, we use the Monte Carlo simulations to argue that several of the apparently wayward points in Fig. 2 are true, non-Gaussian outliers; we eliminate 8 of these outliers and recompute the sample TF properties.

3.1. Slope and Zero-Point Offsets from a Bias-Correcting Analysis

Figs. 2 and 3 illustrate another shortcoming of computing fixed-slope TF offsets from reference distributions. In both figures, the TF relations show some evidence for slope differences. To

describe the TF relations, we require a more complete description of the TF properties of our sample. Luminosity biases introduced by restriction to a magnitude-limited sample, coupled with the intrinsic dispersion in the TF relation, strongly affect the measured slope of the TF distribution (e.g., Willick 1994). At a given velocity width towards the low-mass end of the distribution, only the most luminous galaxies appear in the TF sample. This effect results in a bias towards a shallow measured slope for the “forward” TF relation (where linewidth is the independent variable).

Here, we analyze the *R*-band TF relations of the pair sample and the C97 sample using the luminosity bias correction technique of Willick (1994). For the C97 sample, we eliminate 5 galaxies which do not meet the original selection criteria; 2 are not in the UGC, 2 have UGC diameters $< 1'$ and two have $m_{\text{Zw}} > 15.5$. We omit the correction for diameter limit bias in the C97 sample. This correction increases the measured differences between the C97 TF distribution and the pair relation by a small amount ($\lesssim 2\%$ in the slope and offset and $\sim 3\%$ in the scatter).

We apply the luminosity bias correction closely following Willick (1994). The first step is to relate the selection parameter, in this case the Zwicky magnitude, m_{Zw} , to the TF parameters M and η . We use the functional form adopted in Willick (1994), $m_{\text{Zw}} = a + b\eta + cm$, where a , b , and c are the coefficients we fit and m is the relevant apparent magnitude (R for the pairs, and r for the C97 sample). We use the bias-correcting technique outlined in Sec. 3 of Willick (1994) to fit for a , b , and c , as well as for $\sigma_{M,\text{Zw}}$, the scatter in the relationship. Table 3 lists the results.

Next, we correct for the bias introduced because only galaxies with $m_{\text{Zw}} \leq 15.5$ appear in the samples (C97 and our sample). The technique is iterative. The steps are: (1) estimate the TF parameters, (2) using the relationship between the TF parameters and the selection parameter, m_{Zw} , compute the expectation value of the measured apparent magnitude, m , as a function of η , and correct each point for the difference between this expectation value and the “true” value of m from the TF relationship found in (1); (3) re-compute the TF relationship, and (4) iterate on steps (2) and (3) until the TF slope and offset converge.

In Table 4 we list the TF parameter fits resulting from this technique for the C97 data and for our galaxies in pairs. Because of this bias correction, the slope we measure for the C97 data, -7.03, is steeper than the slope C97 compute, -6.36. Fig. 4 shows the solutions (crosses). The points represent the Monte Carlo results below.

3.2. Computing Confidence Intervals with a Monte Carlo Simulation

We use a Monte Carlo simulation to estimate the confidence levels appropriate for the TF parameter solution. We draw model datasets from the best-fit TF relation (based on the analysis in Sec. 3.1), subject the “data” to the selection effects relevant to each sample, and use the Willick (1994) technique to find the best-fit TF parameters of the simulated data.

To model the TF relation for the pair data, we draw absolute magnitudes, M , from the void galaxy LF of Grogin & Geller (1999) ($M_\star = -20.4$, $\alpha_{\text{LF}} = -1.17$) because Grogin & Geller derive their LF from data of very similar quality based on a survey of similar depth to our pair sample. The Grogin & Geller LF is consistent with the Century Survey LF (Geller et al. 1997).

After drawing M from the LF, we convert to η using the input TF distribution, the solution found via the Willick technique. We then mimic scatter in the forward TF distribution by adding a random number to M generated from a Gaussian distribution with dispersion σ_{TF} , where σ_{TF} is the scatter in the TF distribution measured from the data. We compute the apparent magnitude, m , from M by assigning a randomly drawn velocity appropriate for a fixed-solid-angle survey with $2300 \text{ km s}^{-1} \leq cz \leq 15000 \text{ km s}^{-1}$; we draw a value of m_{Zw} for each point from the relationship $m_{\text{Zw}} = a + b\eta + c m$, derived from the data, with scatter $\sigma_{m, \text{Zw}}$. Finally, we eliminate points with $m_B > 15.5$ to mimic the selection bias.

For the pair study, we draw “datasets” of the appropriate number of galaxies (i.e., 90 for the pair sample and 279 for the C97 sample). We use the Willick (1994) procedure to find the best-fit TF solution for each “dataset”. Fig. 4 shows the results for 1000 simulations of each distribution. The results are centered on the input solution, demonstrating that the Willick (1994) technique properly accounts for luminosity bias.

3.3. Identifying the Outliers to the Pair TF Distribution

Fig. 5 shows the TF distribution of the pair data, along with 3 examples of Monte Carlo realizations. The data and realizations are not a good match: even though we used the *measured* scatter to construct the realizations, the scatter in the realizations substantially exceeds the scatter in the data at the high-mass end. Thus, the observed pair distribution includes a small set of apparent outliers to the TF relation. (By comparison, the Monte Carlo realizations of the C97 data are a much better match in Fig. 6.)

We identify these outliers using a simple sigma clipping algorithm. Because the outliers dominate the slope computation, some assumption about the slope is necessary. We eliminate points by fixing the slope to the value for the C97 distribution without bias correction, -6.36. We use this slope for two reasons: the slope of the observed C97 distribution is applicable to the observed pair distribution because the magnitude limits for the samples are the same, and we seek to keep the prescription simple and easy to implement. In practice, the choice of -6.36 instead of -7.03 does not affect the set of outliers we identify. We eliminate outliers iteratively, by (1) fixing the slope and computing the offset, Δ_{TF} , and dispersion, σ_{TF} , (2) removing the 3σ outliers and the points with error bars extending outside the 3σ region, and returning to (1) until the sample is stable. (We exclude points with error bars outside the 3σ region chiefly in order to exclude one galaxy, UGC 4774, which lies extremely close to the boundary, and is in fact a 2.94σ outlier — this procedure is equivalent to 2.94σ clipping.) In this way, we eliminate 8 outliers to the distribution.

Fig. 7 shows that the Monte Carlo realizations now match the slope and scatter of the non-outlier data very well. These 8/90 outliers represent a relatively high number; for example, TP00 identify only 2/157 outliers (at a somewhat higher 4 – 5- σ level).

Columns (5) – (7) in Table 2 and the 3rd row in Table 4 show the TF properties of these 82 galaxies. We plot the TF parameters of the sample minus the outliers in Fig. 4. The solution for the non-outlier galaxies is closer to the C97 distribution.

Based on the 68.3% confidence errors (see the description of Table 4), the zero points of the TF relations differ very little. The “field” galaxies are 0.22 magnitudes *brighter* (with only 1.4 σ significance). As we show in Sec. 4, most TF deviations expected in interactions would act in the opposite direction: the pair galaxies would appear “overluminous”. Thus, the marginally significant zero-point offset may be unrelated to the interactions.

The conversion from Gunn r to Cousins R of 0.354 magnitudes from Jørgensen (1994) is one source of uncertainty; she reports a scatter of 0.035 magnitudes from a set of 32 standard star measurements, and a color term of $-0.111(g - r)$ for the reverse measure, $R - r$ (which we do not implement). The color term implies that color differences among samples could lead to substantial systematics introduced by the conversion. Frei & Gunn (1994) measure $r - B$ and $R - B$ colors, and find that $r - R$ ranges from 0.31 – 0.33 for ellipticals through irregulars using spectral energy distribution templates. Because of differences in the literature and uncertainties in the color term, errors from this conversion of up to ~ 0.05 magnitudes are possible. In addition, Monte Carlo results suggest that our failure to account for diameter limit bias in the C97 sample could (artificially) decrease the measured zero points by a further ~ 0.06 magnitudes.

The slopes differ more significantly: we find -5.58 for the pairs with outliers removed and -7.03 for the complete C97 sample; the difference is 1.45 with a nominal 2.6 σ significance. The actual significance of this slope difference is probably greater because our slope-constrained outlier clipping forces the slopes to agree. The choice of fixed slope for clipping forces the pair slope to steepen and, if applied to the C97 sample, would force the C97 slope to become shallower. In spite of these ambiguities, the pair TF parameters are relatively stable to our choice of 3 σ clipping. Even when we clip by 2 σ , removing 14 of the galaxies, the pair TF slope steepens by ~ 0.32 , or $< 1\sigma$.

Additional arguments support the difference between the C97 and pair TF distributions: (1) the pair distribution outliers are twice as frequent as the C97 “outliers”: 9% of the pair galaxies are $\geq 2.9\sigma$ outliers, compared with 4% (11/279) of the C97 galaxies [compared with an expected $\leq 5/297$ outliers from the Monte Carlo simulations, with 99% confidence]. More important, (2) the pair outliers are apparently “overluminous”, whereas 10/11 of the C97 “outliers” (which we do not remove for our computations) lie below the TF distribution. Figs. 6 and 7 thus highlight the true differences in the TF distributions.

In summary, the C97 and pair TF distributions differ somewhat; the outliers and the modest slope differences provide the strongest clues to the true differences. We discuss the implications of

the slope differences in Sec. 5.2.

The outliers have important implications for the study of the TF properties of interacting galaxies and for TF studies of galaxies at high redshift where the detailed properties of the galaxies may be unknown. Next, we explore the physical origin of these outliers which may result from luminosity evolution *or* from errors in the measurement and/or interpretation of the TF parameters.

4. Scatter and Offset in the TF Relation

Several studies use the TF relation as a measure of cosmological luminosity evolution (e.g., Vogt et al. 1996, 1997; Simard & Pritchett 1998). However, luminosity evolution is not the only factor affecting the TF properties of a galaxy. The physical processes which cause substantial luminosity boosts may affect the TF parameters in other ways. If these processes are at work during galaxy interactions, the perturbed galaxies may depart from the TF relation, at least temporarily, due to factors other than or in addition to a luminosity boost (before perhaps resettling onto the relation).

In this section, we start with the most the obvious cases of deviations from the TF relation, the outliers (Sec. 3.2), and explore the clues to their physical origin. We label these outliers “A” — “H” in Fig. 2 and we list their properties in Table 5. We show their images, rotation curves, and surface brightness profiles in Figs. 8 and 9. In Secs. 4.1 – 4.3, we consider the *potential* effects of the interaction on galaxy TF parameters, and discuss the outliers in light of these effects. We summarize in Sec. 4.4.

The effects include: (1) galaxy overlap, which may make separate magnitudes difficult to measure, (2) peculiar velocities, (3) tidal stretching, which pulls flux below the surface brightness limit, artificially elongates a face-on galaxy to appear more edge-on than it really is and affects our ability to measure the photometric inclination, or affects measurements of the disk scale length, needed to compute the C97 $V_{2.2}$ velocity-width statistic, (4) kinematic distortion, which results in a distorted or truncated rotation curve, and (5) a luminosity boost from star formation associated with the interaction.

Effects (1) and (2) introduce measurement errors which are relatively straightforward to estimate (see Sec. 2.3) — we include these effects in the magnitude errors. They may increase the general scatter in the TF distribution, but they are not responsible for the outliers. Effects (3) and (4) are more elusive; we group them into the category of “parameter misinterpretation errors”. These errors occur when measurements of galaxy properties do not represent the same physical quantities that they would for an isolated galaxy in equilibrium. For example, a close galaxy-galaxy pass may distort a galaxy so that the measured kinematics reflect the transient phenomenon, not the gravitational potential of the galaxy. *The error bars do not reflect parameter misinterpretation errors.* We discuss the contributions from these errors below.

4.1. Tidal Distortion

Tidal elongation affects the TF properties of the interacting galaxies. Franx & de Zeeuw (1992) describe the way moderately elongated galaxies (with triaxial or prolate dark matter halos) affect the TF relation (see also Beauvais & Bothun 1999; Bershady & Anderson 2000). However, they restrict their analysis to galaxies with small intrinsic elongations; we require an estimate of the effects of large elongations on photometric parameters.

To illustrate the effects from tidal distortion, we use results from the numerical simulation of Barton, Bromley, & Geller (1999), who demonstrate the effects of this transient distortion on galaxy rotation curves. Fig. 10 shows a simulation of an interacting galaxy from Barton et al. (1999); it is a “Milky Way B” model (see Kuijken & Dubinski 1995), with an intermediate halo size and moderate impact parameter, after a prograde encounter with an equal-mass galaxy. Here, we examine the “toy” model, with 100,000 particles per disk, rather than the fully self-consistent model. We choose this timestep because the kinematic and morphological distortions are dramatic. The initial model is a stable, axi-symmetric exponential disk.

The simulation in Fig. 10 is face-on — the “true” inclination angle is $\sim 0^\circ$. However, the tidal interaction elongates the galaxy. In Fig. 11 we show the results of applying the photometry software to the initial galaxy (circles) and the galaxy in Fig. 10 (triangles). Open points show ellipses fit by the program; closed points show ellipses fixed by the program or that represent non-convergent fits. Although Fig. 11 applies to only one timestep in one simulation, it shows a relatively strong tidal distortion and should represent an approximate upper limit to the distortion introduced by a tidal encounter.

The tidal stretching has little effect on the observed total (face-on) magnitude of the galaxy — only the fainter parts of the outer disk depart from the initial galaxy. A stronger encounter could do more damage, but it might affect the morphology of the galaxy enough to exclude it from a sample of disk galaxies. Similarly, the surface brightness profile, hence the face-on measured disk scale length, remains regular, in part because the program allows the position angles and ellipticities to vary as a function of radius.

The effects of the interaction on the intrinsic ellipticity of the galaxy, which we define as the ellipticity of the galaxy when viewed face on, are much more apparent. The ellipticity reaches 0.4885, corresponding to an inferred inclination of 60.9° (compared to a true inclination of 0°). This elongated galaxy would appear in our TF sample, but it would have a velocity width near zero and would therefore be an apparently overluminous outlier to the TF distribution.

In Fig. 12 we show the offset in the velocity width, η , which results from tidal elongation. We compute $\Delta\eta$ assuming ~ 2600 observation angles spaced uniformly about the unit circle. For the calculation, we assume a thin, elliptical disk, compute the projected figure of the ellipse, and measure the position angle misalignment of the major axis, and the inclination, i_{meas} . Because we use the thin disk approximation, we compute with the simple formula $\cos(i_{\text{meas}}) = \frac{b}{a}$, where a

and b are the maximum and minimum diameter of the projected figure. We require $i_{\text{meas}} > 40^\circ$ to include the “galaxy”; we compute $\Delta\eta = \log[\sin(i_{\text{true}})/\sin(i_{\text{meas}})] + \log(f_{\text{align}})$, where f_{align} is the error introduced by the position angle mismeasurement (see Equation 1).

Any errors in η due directly to inclination mismeasurement from a non-zero intrinsic ellipticity are accompanied by small errors in absolute magnitude due to an incorrect inferred reddening correction, and larger errors in the measured disk scale length, which Fig. 13 describes for idealized ellipses. These have more minor (second order) effects on the measured TF parameters.

Tidal elongation introduces appreciable errors only in extreme cases. The second panel in Fig. 12 is appropriate for the simulated galaxy in Fig. 10. Even for this extreme example, errors in η would exceed 0.3 dex only 24% of the time. Furthermore, these distortions are short-lived (\lesssim a few hundred Myr). Because we sample pairs both before *and* after a close pass, at most \sim half of the sample could be post-close-pass. In addition, these features are only associated with strong, prograde interactions, which will occur only a small fraction of the time (\ll half).

We conclude that only a small number of outliers ($\lesssim 3\%$) would result from the elongation effects of tidal forces. They should have tidal-tail morphology. Of the outliers in Figs. 8 and 9, only UGC 6994 has the distinctly tidal “grand-design” structure; it is therefore the best candidate for inclination mismeasurement due to tidal distortion. Because tidal distortion is unlikely to affect η , the other galaxies are probably outliers for other reasons.

4.2. Kinematic Distortion, Truncation, and Narrow Emission Line Galaxies

Fig. 1 of Barton et al. (1999) shows the transient kinematic signatures of tidal distortion produced in simulations of dissipationless interactions. The figure generally includes the most extreme timestep in each simulation, and therefore represents an approximate upper limit to the distortion in the models. We estimate $V_{2.2}$ from the simulations using the original disk scale length (one length unit in the simulations). Because the C97 rotation curve model provides a very poor fit to these curves, we measure the velocity width directly (i.e., without use of the model), by interpolating points in the vicinity of $2.15 R_{\text{disk}}$. Most of the departures from the undisturbed model ($V_{2.2} \approx 1.8$) result from the dips in the rotation curves. The deviations in the TF parameter, η , resulting from these distortions range from -0.11 to 0.07 dex for these nine simulations, with a median of -0.07 dex. If these relatively centrally concentrated models represent typical galaxies, the expected deviation from the TF relation due to dissipationless effects on well-sampled rotation curves is very small.

Gasdynamical effects on the measured kinematics are much more uncertain. Close passes between galaxies initiate gas infall (e.g., Mihos & Hernquist 1996) which BGK detect as central star formation. The effects of the infall on $\text{H}\alpha$ kinematics are difficult to estimate due to uncertainties in the hydrodynamical prescriptions adopted in numerical simulations. A comparison between stellar and gas kinematics in individual galaxies would aid in estimating the magnitude

of this effect.

Non-uniformity in the spatial distribution of the ionized gas is probably the most substantial cause of errors in linewidth interpretation. If the gas is concentrated in the center of a galaxy (as expected after a close pass), or in lumpy emission on only one side of the galaxy, the rotation curve will not be well sampled. These effects generally result in an underestimate of the velocity width.

We can estimate the importance of non-uniform H α emission in individual cases. NGC 7253B is an obvious example — only a fraction of the rotation curve is sampled, presumably because the slit fell on only one (extended) emission line region. The rotation curves of the outliers in Fig. 9 all appear truncated; this truncation may result in underestimated velocity widths (e.g., Verheijen 1997). Four our outliers, the truncation results from the concentration of emission line gas in the centers of the galaxies. Next, we describe the properties of these outliers in detail.

4.2.1. *The Low-Mass Outliers — Counterparts to Narrow Emission Line Systems at High Redshift?*

The four low-mass outliers in our study share several properties. Table 5 and Fig. 9 illustrate that these four low-luminosity TF outliers are compact and relatively blue, with either substantial ongoing star formation or Balmer absorption. The $B - R$ colors dip in or near the centers of the galaxies, suggesting that the star formation is centrally concentrated, as expected based on simulations of interacting galaxies (e.g., Mihos & Hernquist 1996).

Fig. 9 shows that the rotation curves do not flatten substantially. Spatially extended, two-dimensional velocity mapping of the galaxies would determine whether they lie on the TF relation. Only UGC 8919N has existing spatially-resolved HI observations.

UGC 7085W has a rotation curve that extends only a few arcseconds. It is irregularly shaped, and its colors and EW(H α) show evidence for recent star formation.

NGC 2719A consists of a faint, irregular disk of emission with three bright HII regions. The rotation curve only traces the disk well on one side; the emission is dominated by the bright knots.

UGC 8919N has little H α emission and no obvious signs of tidal distortion. As the emission extends only $\sim 5 - 10''$ from the center, the rotation curve may only include a bar. Archival C and D configuration VLA observations (P.I.: J. Chengalur) allow us to separate the HI flux of this minor companion to UGC 8919. Although the flux is spatially unresolved, the profile width (at 20% of maximum) is a factor of ~ 2 wider than our measurement of the rotation curve indicating that in this case, *UGC 8919N lies on the radio TF relation*, and appears as an outlier in our plot only because the truncated optical rotation curve does not reflect the mass of the galaxy.

CGCG 132-062, has a distinct S0 morphology with a very blue bulge ($B - R \sim 0.6$, uncorrected for extinction). It has a very small half-light radius ($0.95 h^{-1}$ kpc). Again, the rotation curve is

not spatially well-extended (only $8'' - 15.3''$) and may fail to describe the velocity width of the disk. If parameter errors are not responsible for boosting NGC 2719A and CGCG 132-062 off the TF relation, as they are in the case of UGC 8919, a combination of star formation and/or substantial morphological evolution could be responsible.

The compact, blue galaxies at intermediate redshift (Phillips et al. 1997), including the compact narrow emission line galaxies (Koo et al. 1994; Koo et al. 1995; Guzmán et al. 1997; Guzmán et al. 1998; CNELGs hereafter), may be similar to these low-mass outliers. The CNELGs are barely-resolved, heavily star-forming galaxies found at redshifts $0.1 \leq z \leq 1.6$; CNELGs are very compact, with half-light radii from $\sim 1-4$ kpc (see Koo et al. 1994; 1995). Their status is currently debated — they may be the spiral galaxy bulges in formation (Kobulnicky & Zaritsky 1999), or a bursting population that will fade to present-day dwarf galaxies. To date, the narrow line widths of these galaxies ($28 - 157$ km s $^{-1}$, with many < 65 km s $^{-1}$) provide the strongest evidence in favor of the dwarf hypothesis.

However, at least one of our 4 low-mass outliers represents a galaxy with a resolved emission line rotation width that does not represent its kinematic mass (outlier “C”, UGC 8919N, with archival VLA observations; Barton & van Zee 2000). Because the properties of our outliers are strikingly similar to those of the lower luminosity compact objects in the Hubble deep field (Phillips et al. 1997) and the CNELGs, they may represent systems in similar physical states. In particular, both the nearby TF outliers and the CNELGs may represent cases in which a close pass or other non-axisymmetric perturbations caused gas infall and subsequent star formation. The narrow line widths and compact morphologies at intermediate redshift would result from strong star formation confined to only the inner few kpc of the galaxies, during an epoch of bulge enhancement.

4.3. Luminosity Evolution

In Fig. 14 we show the effects of added flux from star formation in the R band. We plot the C97 R relation; the contours show the shift produced by a burst of absolute magnitude M in the TF properties of the galaxies, *assuming the only effect of the burst is luminosity evolution*. The figure highlights two very important facets of the TF relation as a measure of luminosity evolution. First, the relation is steep and has a large scatter; hence, only a large burst results in an appreciable residual. Second, the Tully-Fisher relation is a relation in log space. It measures fractional changes in luminosity and velocity width. As Fig. 14 illustrates, the high-mass end of the TF relation is insensitive to all but the very brightest bursts of star formation, which are unlikely given the gas content of nearby bright galaxies. Therefore, we expect local bursts of star formation to result in *slope* changes. Furthermore, it is not *a priori* obvious whether evolution at high redshift would increase the luminosity of galaxies at a constant fractional rate: Simard & Pritchett (1998) find some evidence for TF slope changes at intermediate redshift while Vogt et al. (1997) do not.

Barton et al. (2000a) detail the evidence for interaction-triggered star formation in the centers of many of the pair galaxies. Here, we estimate the magnitude of the luminosity boost we expect from central star formation in our sample. The existing data only provide an estimate of the total amount of recent (≤ 1 Gyr) star formation *in the galaxy centers*. Barton et al. (2000b) describe these estimates in detail; here, we summarize the results.

Fig. 15 shows the parameters of the central bursts of star formation for 89 of the pair galaxies (one is absent from the BGK spectroscopic sample). We use photometry in the spectroscopic apertures (typically only $\lesssim 1 \text{ h}^{-1} \text{ kpc} \times \text{a few } \text{h}^{-1} \text{ kpc}$) to compute $B - R$ colors, which we correct for reddening based on the Balmer decrement. The contours are lines of constant R -band burst strength and age. We use the Starburst99 models (Leitherer et al. 1999) to compute these parameters. We assume that all the $\text{H}\alpha$ flux comes from a recent, new burst of star formation, which proceeds at a constant star formation rate with a Miller-Scalo initial mass function (IMF) and solar metallicity. We assume $B - R = 1.5$ for the central pre-burst population (see Barton et al. 2000b). Assuming that the galaxy was on the C97 TF relation before the star formation began, we list the central burst strengths (fraction of R -band flux), and luminosities in Table 6, along with the “expected” TF residual from this central burst. We compute this expected residual assuming that the galaxy lay on the C97 TF relation before being boosted by star formation with luminosity $M_{R,\text{burst,slit}}$.

For all of the outliers, the expected boost from the central star formation we measure is substantially smaller than the measured residual (column 6). Although the spectroscopic aperture misses much of the flux of the galaxy (see column 4), we expect frequent centrally concentrated star formation (e.g., Mihos & Hernquist 1996). This central star formation it is not primarily responsible for the set of outliers we detect, although it may be responsible for the discrepancies between the C97 “field” TF relation and the relation for the non-outlier pair galaxies.

4.4. Summary of the Outliers

In sections 4.2 and 4.3, we suggest physical origins for the TF residuals of 6 of the 8 outliers. With the exception of the elongated UGC 6944, and possibly UGC 312E, our arguments imply that neither morphological distortions nor dissipationless kinematic distortions have strong effects on the TF properties of these galaxies. Nor does central star formation contribute enough flux to explain the outliers. The remaining explanations for the outliers are dissipative effects on the rotation curve (gas infall and non-uniform or truncated emission) and disk star formation. In 5 cases, rotation curve distortion leads us to suspect dissipative effects on the rotation curve. Four of these galaxies are low-mass outliers with truncated rotation curves that share several properties. We identify this class of objects with the compact, blue galaxies at high redshift (Sec. 4.2.1). Finally, two of the outliers are ambiguous; we discuss these galaxies below. We summarize these conclusions in Column 7 of Table 6.

UGC 4774 is the only apparently underluminous outlier, and as such, it is the most difficult to explain. Parameter errors could only result from: (1) underestimating the inclination, which would move the galaxy at most 0.034 dex in the $-x$ direction on Fig. 2 due to velocity projection and 0.3 magnitudes in the $+y$ direction due to an underestimate of the internal extinction (based on the C97 prescription), (2) over-estimating the velocity width, which is unlikely given the well-sampled rotation curve, (3) missing significant flux. Its scale length, $8.1 \text{ h}^{-1} \text{ kpc}$, is among the largest in the sample, and reflects the tidal stretching — all four galaxies with scale lengths $> 8 \text{ h}^{-1} \text{ kpc}$ have distinct tidal tails. However, Sec. 4.2 demonstrates the difficulty of missing significant flux ($\geq 40\%$) from this effect. The final possibility is (4) under-estimating the Hubble-flow velocity (i.e., if its true recession velocity is closer to 3000 km s^{-1} than the measured 2330 km s^{-1}). UGC 4774 is near the close edge of a void, and may be flowing away from the void and towards the Milky Way, but its TF residual requires an unlikely peculiar velocity of at least 600 km s^{-1} to shift it half a magnitude. As each single possibility is unlikely to result in a large shift, the cause for its TF residual is either a combination of these factors or an unknown, and more fundamental physical difference from the other galaxies.

UGC 312E is also ambiguous. Although it shows no evidence for tidal tails, it may still be tidally distorted. Its residual may also result from several effects added together, possibly including an underestimate of the scale length and inclination, and/or star formation in the outskirts of the disk (not included in the spectroscopic aperture, hence missing from Table 6).

5. Exploring the Origin of the Slope Offset: the Non-Outlier Data

In Sec. 4, we explore the expected effects of tidal distortion and star formation on the TF relation for galaxies in pairs. Here, we apply empirical tests for correlations between the TF residuals and various measures of interaction-triggered distortion in the non-outlier data.

If the third parameter depends on luminosity and velocity width, identifying correlations between TF residuals and third parameters is difficult: both systematic errors in the slope of the relation and selection effects can easily give rise to false correlations. For example, Zaritsky & Rix (1997) report a correlation between photometric asymmetry and the residual from the Pierce & Tully (1992) B -band TF relation (panel B of Fig. 16); the correlation might result from increased star formation in asymmetric galaxies (see Rudnick, Rix, & Kennicutt 2000). If real, this conclusion would be discrepant with our results (Sec. 5.1). However, the correlation is an artifact. Panel C of Fig. 16 shows the relationship between the B -band TF residual from the Pierce & Tully (1992) relation and the velocity width. The figure shows a clear systematic difference between the Pierce & Tully TF relation and the TF relation appropriate for the Zaritsky & Rix data. The TF residuals are correlated with the velocity width, W^i ; the correlation is highly significant — a Spearman rank test indicates a likelihood of no correlation of $P_{\text{SR}} = 3 \times 10^{-10}$. Panel A shows the correlation between the asymmetry parameter and the velocity width of the galaxy, which reflects a fundamental physical property of spiral galaxies — that low-mass galaxies

are more asymmetric. This correlation is also significant ($P_{SR} = 0.018$). Finally, Panel B shows the correlation Zaritsky & Rix report between the residual from the Pierce & Tully (1992) B TF relation and the stellar asymmetry of the I -band light. *The correlations in panels A and C give rise to the apparent correlation in panel B.* The solid line is the least-squares fit to the data points in panel B; the dotted line coincident with the solid line is the combination of the fits in panels A and C. The scatters match well ($\sigma_A = 0.072$, $\sigma_C = 0.11 \text{ km s}^{-1}$, $\sigma_B = 0.073 \approx \sqrt{\sigma_A^2 + (b_A \sigma_C)^2}$, where $b_A = -0.15 \text{ km}^{-1} \text{ s}$ is the slope of the fit in panel A). When we remove the systematic TF slope problem by fitting the correlation in panel C, the correlation between the TF residual and the asymmetry disappears ($P_{SR} = 0.70$).

A false correlation between the TF residuals and a third parameter can arise only if the third parameter depends on η and M . False correlations can have two distinct (but related) causes: systematic slope errors and selection effects. The Zaritsky & Rix example involves a systematic slope error. With the proper slope, this false correlation disappears. We address this concern in our study by testing for correlations using three different slopes: the C97 slope (as measured by C97), -6.36, the non-outlier pairs slope derived with the Willick (1994) technique, -5.58, and the non-outlier pairs slope derived from direct least-squares fitting, -4.75. The last two rows of Table 7 show that using the steepest slope results in no correlation between the residuals and M_R and that using the shallowest slope results in no correlation between the residuals and η .

Selection effects are more complicated; they can give rise to false correlations if the third parameter combines with one or both of η and M to influence sample selection. For example, we analyze the R -band TF relation for a B -selected sample of galaxies (from the Zwicky catalog). Therefore, the $B - R$ color influences the selection of intrinsically faint galaxies — faint red galaxies are absent from our sample. Even without a correlation between the TF residual and the color of a galaxy, the sample selection results in a false correlation because of the scatter in the TF relation. “Underluminous” red galaxies are underrepresented, and the blue galaxies will seem preferentially underluminous. In fact, we see no trend with color, suggesting that this effect is either very small or, more likely, that excess star formation cancels it. This bias would damp any tendency for blue galaxies to appear overluminous due to excess star formation.

These arguments suggest that false third parameter correlations should have some distinguishable characteristics. A correlation may be false if it doesn’t persist for different slope values. In addition, a correlation is particularly suspicious if the third parameter is a strong function of both M and η . In this case, the correlation may still be real, especially if it persists for multiple slope choices. (Note, however, that if a third parameter/residual correlation is real, the third parameter should correlate with *either* M or η , by definition, if the correlation is strong enough.) Conversely, the failure to detect a correlation does not mean that it is entirely absent. Both large scatter in the intrinsic TF distribution and a large scatter in the relationship between the third parameter and the residual associated with the parameter can mask the true correlation. We apply these arguments in the analysis below to distinguish between false and true correlations.

5.1. Searching for Third-Parameter Dependence in the TF Relation

In this section, we describe several statistics or measures, both discrete and continuous, which we use to test for correlations between the TF residuals and the amount of tidal and kinematic distortion and star formation in each galaxy. Tables 7 and 8 list the continuous and discrete statistics, respectively, which we describe below. We exclude the 8 outliers from this analysis; they would otherwise dominate the results. We list their parameters separately in Table 9.

5.1.1. Measures of Distortion and Star Formation

Objective measures of tidal or kinematic distortion are difficult to define (Abraham et al. 1994; Odewahn et al. 1996; Windhorst et al. 1999; Conselice, Bershady, & Gallagher 2000; Conselice, Bershady, & Jangren 2000; Bershady, Jangren, & Conselice 2000); these measures are very sensitive to the exact surface brightness of the tidal features. Our statistics and measures are not exhaustive descriptions of the galaxy; they provide estimates of the amount of distortion present.

Rotation Curve Distortion: We consider two statistics which measure the amount of rotation curve distortion. In Table 7, we list an objective measure, χ_{rc}^2 , the χ^2 per degree of freedom of the fit to the (empirical) rotation curve model of Courteau (1997). In addition, we divide the sample based on our estimate of the amount of rotation curve distortion; we list this statistic in Table 8. We classify the galaxies with “normal”, “marginal”, and “distorted” rotation without *a priori* knowledge of their placement on the TF relation.

Fig. 17 shows examples of the three classes of rotation curves. The figure shows an image, surface brightness profile and rotation curve of NGC 4134, which has a “normal” rotation curve. We also show a “marginal” case, UGC 4383N; the rotation curve barely turns over, providing essentially a lower limit to V_c . Finally, Fig. 17 shows NGC 4615, which is significantly distorted, even though NGC 4615 is not an outlier to the TF relation. Although this judgment-based measure gives a somewhat different picture of the effects of rotation curve distortion from the more objective χ_{rc}^2 , the mean reduced χ^2 values from the fits to the C97 functions are 4.1, 8.8, and 12.7, respectively, for the 40 “normal” curves, 37 “marginal” curves, and 13 “distorted” curves.

Rotation Curve Truncation: Our continuous measure of rotation curve truncation is the maximum extent of the rotation curve (R_{max}) divided by the disk scale length, R_{disk} . Galaxies with large values of $R_{\text{max}}/R_{\text{disk}}$ have well-sampled rotation curves.

Morphological Distortion: We include 4 separate measures of morphological distortion in the tables. The continuous morphological distortion measures are (1) R_{disk} , the disk scale length, which can serve as a measure of tidal stretching — the few galaxies with the most prominent tidal tails have very large values of R_{disk} ; and (2) χ_{phot}^2 , the χ^2 per degree of freedom for the linear fit to the surface brightness profile of the outer disk (computed based on the ellipse fits, where the

center, inclination, and position angle are allowed to vary with radius).

We also include two discrete measures of morphological distortion. The first is a “by-eye” description of the disk as “normal”, “distorted” or “ambiguous”. We compare only the “normal” and “distorted” cases in Table 8. This judgment-based statistic is more sensitive than χ^2_{phot} to relatively faint tidal features. Some galaxies which appear distorted have low values of χ^2_{phot} ; in most cases, the “by-eye” measure is effective. The final morphology measure is based on the measure of the ellipticity, ϵ , of the galaxy’s disk, and hence its inclination. We describe the procedure for estimating the error, σ_ϵ , in Sec. 2.4. Galaxies with stable, fit values of ϵ in their outer isophotes and $\sigma_\epsilon < 0.05$ are in the “well-defined ϵ ” sample; galaxies with less stable values ($\sigma_\epsilon > 0.05$) are in the “poor ϵ ” sample. The “no-fit ϵ ” sample consists of galaxies for which we can not fit ellipses at $\mu_R \geq 24.5$; it includes many of the most distorted galaxies (although it excludes the few cases where the galaxy was fit by hand, typically classified as “good ϵ ” galaxies).

Star Formation: In Table 7 we list 4 measures of recent star formation: the $\text{EW}(\text{H}\alpha)$, which measures the most recent star formation, the color of the entire galaxy [corrected for reddening with the Courteau (1996) prescriptions], the color of the center of the galaxy in the spectroscopic aperture of the BGK observations (corrected for reddening based on the Balmer decrement), and the strength of the new burst of star formation in R (see Sec. 4.3).

Star/Galaxy Overlap: Finally, we divide the sample based on potential problems with the photometry. We consider galaxies which overlap their partners, and galaxies with substantial contamination from stars. Two galaxies suffer from both, and are included in both subsamples.

5.1.2. Searching for TF Residual Dependencies

Tables 7 and 8 both describe the results of statistical tests for third-parameter dependence in the TF relation. For the continuous measures (Table 7) and for three TF slopes, columns 3 – 5 list the Spearman rank probabilities of no correlation between the TF residuals and the third parameter. In columns 7 and 8, we list the Spearman rank probabilities of no correlation between each third parameter and the TF parameters: the velocity width, η , and the total magnitude, M_R , respectively. We list the correlations between the TF parameters and the residuals in the last two rows.

The only possible correlations with TF residuals and the continuous third parameters (columns 3 – 5 of upper rows, Table 7) are for $B - R$ color and R_{disk} . Both color and R_{disk} correlate strongly with *both* η and M_R , raising the possibility that the correlations with the TF residuals may result from the dependence of the residuals on η and M_R . The correlations with TF residuals appear only for some slopes, supporting that conclusion. R_{disk} correlates extremely strongly with M_R ; it is suspicious that the strongest TF residual correlation is for a slope of -4.75, which is the slope that results in the strongest correlation between M_R and the residuals. Similarly, $B - R$ is strongly correlated with η . The TF residual/ $B - R$ correlation is strong only

for the steep slope, which has the largest η residuals. Therefore, we conclude that the apparent correlations between residuals and both R_{disk} and global color are probably false.

For the discrete measures (Table 8), columns 5 – 7 list the Kolmogorov-Smirnov probabilities of the null hypothesis that the distributions of TF residuals for subsamples broken down based on the third parameters have been drawn from the same distributions. In columns 8 and 9 we consider the distributions of η and M_R instead of the TF residuals. The only significant differences in TF residual distributions appear between galaxies with “normal” kinematics and galaxies with “distorted” kinematics. For the least-squares slope, -4.75, the 9 galaxies with “distorted” rotation curves are “overluminous”, with an average residual of -0.44 magnitudes using the least-squares TF intercept, -20.98 magnitudes. In addition, there are no differences in the η distributions, and at best only minor differences in the M_R distributions (possibly due to the more fundamental TF residual dependence). Therefore, we conclude that strong *kinematic* distortion is a significant predictor of TF residuals. The required level of distortion appears in only 9 of the 82 non-outlier galaxies, but it appears in 4 of the 8 outliers (see Table 9), further supporting our conclusion.

5.2. The Bottom Line: Luminosity Evolution Contributes to the Slope Offset

In Sec. 3.3, we measure a slope difference between the (non-outlier) pair galaxies and the C97 sample. In Sec. 4, we argue that star formation and kinematic distortion have the largest effects on the TF properties of these galaxies. Although we detect differences in the TF residuals based on kinematic distortion, the 9 distorted galaxies do not cause the slope offset: if we remove these 9 points and repeat the Willick (1994) procedure, using the Monte Carlo simulation to compute confidence intervals, the measured slope and offset stay nearly the same: $\Delta_{\text{TF}} = -20.56 \pm 0.14$, $\alpha_{\text{TF}} = -5.71 \pm 0.47$, and $\sigma_{\text{TF}} = 0.53 \pm 0.070$. There is still a 2.5σ difference between the pairs slope and the C97 slope (-7.03 ± 0.26).

Central star formation certainly contributes to the flux of these galaxies, especially at the low-mass end (see, e.g., column 5 of Table 6). In Sec. 5.0, we argue that selection effects can damp the expected color dependence in the TF residuals caused by star formation. A large scatter in the colors of the pre-interaction galaxies will also damp this expected dependence. Therefore, in spite of our failure to detect a color-residual dependence, we conclude that star formation is probably a substantial contributor to the differences between the TF properties of our sample and the C97 sample.

Table 7 shows that the burst strength, s_R , correlates with velocity width ($P_{\text{SR}} = 0.055$) and luminosity ($P_{\text{SR}} = 0.007$); lower-mass galaxies have stronger bursts of star formation. We measure s_R in only the central region of the galaxy; the burst flux in this region provides a lower limit to the total R -band magnitude change due to the burst: $\Delta M_L = 2.5 \log(1 - f_{\text{slit}} s_R)$, where f_{slit} is the fraction of the R flux incident on the spectroscopic aperture (e.g., column 4 of Table 6). The burst is probably strongest in the central region. Therefore, the magnitude change assuming

a constant burst strength throughout the galaxy (from disk star formation) is an upper limit: $\Delta M_U = 2.5 \log(1 - s_R)$, which is only well-defined for $s_R < 1$. (Note that this quantity is different from the quantity in column 5 of Table 6, for which we assume that the galaxy lies on the C97 TF without the burst.) For the Miller-Scalo IMF with constant star formation and an assumed old population with color $B - R = 1.5$, Fig. 18 shows the range of possible burst “corrections” to the TF properties of the sample. For galaxies with $0 < s_R < 1$ (solid points), we show the lower-limit “correction” for the central burst only (horizontal line) and the upper-limit “correction” assuming a constant burst strength (arrow). Most of the high-mass galaxies are firmly anchored (but two high-mass exceptions have $s_R = 1$, the starred points). However, star formation can affect the low-mass galaxies substantially. The range of possible corrections for the low-mass galaxies is large, allowing for substantial steepening of the slope with subtraction of the recent star formation.

We estimate the upper limit of the effects of triggered star formation on the low-mass galaxies empirically from our TF results, assuming the differences between the C97 TF and the non-outlier pair TF at the low-mass end are entirely due to star formation. The relations intersect at $\eta_* = -0.155$; for $\eta \leq \eta_*$, a pair galaxy luminosity is greater than that of a typical C97 galaxy. The increase in flux is equal to $\delta M = 1.45(\eta_* - \eta)$, a boost of 0.35 magnitudes, or 39% in flux, at the low-mass end, $\eta = -0.4$. These values correspond to *average* bursts of up to -17.1 magnitudes in R . This burst size is very sensitive to the measured zero-point offset. If the true zero-point of the C97 relation is 0.1 magnitudes fainter (see Sec. 3.3), we expect average bursts of up to $M_R = -17.7$.

Bursts in this size range would be undetectable at the high-mass end of the TF relation (see Fig. 14). The Leitherer et al. (1999) models (with solar metallicity) show that constant star formation rates of $\sim 0.5 - 2.6 M_\odot \text{ yr}^{-1}$ for 10^7 years or, much more likely, $\sim 0.2 - 0.4 M_\odot \text{ yr}^{-1}$ for 10^8 years (see Barton et al. 2000a), can form enough new stars to account for $M_{\text{burst}} = -17.1$, where the range of values results from the the range of stellar initial mass functions in the models. With a 0.1-magnitude increase in the measured C97 R -band zero point (due to r -to- R conversion errors or correction for diameter limit bias), these star formation rates can nearly double and still be consistent with the data. Only a fraction of the galaxies in our sample are undergoing triggered star formation; thus the actual change in slope due to star formation probably results from stronger bursts in fewer than half of the galaxies. Our bursts of $\lesssim 0.5$ magnitudes are marginally significant and the constraints this technique places on their strengths are only statistical in nature.

6. Detecting Star Formation at High Redshift

The cosmological assembly of galaxies at very high redshift and the subsequent variations of the star formation rate as a function of redshift are constraints for galaxy evolution (e.g., Kauffmann & White 1993; Somerville & Primack 1999; Kolatt et al. 1999). The TF relation provides an important tool for measuring these effects. Hierarchical models predict an increased rate of

mergers and interactions at high redshift, borne out by observations of an increased incidence of irregular morphology at high redshift (Abraham et al. 1994; van den Bergh et al. 1996; Odewahn et al. 1996). Our study focuses on the best objectively-selected candidates for evolving galaxies at the current epoch: galaxies in pairs. Although minor mergers are absent from our sample, the processes by which minor mergers trigger gas infall and star formation (e.g., Mihos & Hernquist 1994) are qualitatively similar to the triggering processes in major interactions. Our results are broadly applicable as a baseline for TF studies of evolving galaxies at high redshift.

The potential for TF outliers and for greater scatter increases the amount of data necessary to detect an elevation in the star formation rate at high redshift. Some outliers can be eliminated based on kinematic distortion observable even at high redshift (e.g., NGC 7235B in Fig. 8). However, most are more difficult to prune on this basis. Any high-redshift TF study should include enough data in each redshift range to define a locus for typical galaxies and to eliminate the outliers.

Approximately 90% of the pair galaxies in our sample lie reasonably close to the TF relation of C97. Thus, even if the slope and offset deviations in our sample are due entirely to “parameter misinterpretation errors” (which they are not), tidal distortions are relatively ineffectual. High-redshift samples the size of this study should be able to detect luminosity evolution $\gtrsim 0.5$ magnitudes or better at R , even if the samples include interacting galaxies.

Although longer rest-frame wavelengths like R are reliable due to small scatter and less sensitivity to very recent star formation, observational considerations frequently make studies of the rest-frame B TF properties more convenient. We apply the Willick (1994) technique to the B -band data [corrected for extinction with the Courteau (1996) prescriptions, with corrections 4/2.2 times larger in B]. With no outlier clipping, we find TF parameters $(\Delta_{\text{TF}}, \alpha_{\text{TF}}, \sigma_{\text{TF}}) = (-18.94, -3.02, 1.01)$. Clipping with the Tully & Pierce (2000) B -band slope of -7.27 yields 8 outliers; 7 are the same as the R -band outliers, including all of the low-mass outliers. The “underluminous” UGC 4744 is not a B outlier, and the very blue Northern half of NGC 3991 is, with (corrected) $B - R = 0.33$. With these 8 outliers removed, we find B -band TF parameters $(\Delta_{\text{TF}}, \alpha_{\text{TF}}, \sigma_{\text{TF}}) = (-19.33, -4.88, 0.68)$.

The set of outliers identified in a high redshift study should contain some of the most interesting objects, presumably including anomalously narrow emission line galaxies (like the CNELGs). The relatively high incidence of these objects in our pair sample occurs because of close galaxy-galaxy passes, which can drive a large fraction of the disk gas into the galaxy center. The stars formed may contribute to the bulge. Thus, TF studies where sample pruning is minimized may provide a powerful means of selecting galaxies evolving along the Hubble sequence.

7. Conclusion

We use optical emission line rotation curves to investigate the R -band Tully-Fisher properties of a sample of 90 spiral galaxies in close pairs. The sample includes a range of luminosities, morphological types, and degrees of tidal distortion. With the exception of eight distinct $\sim 3\sigma$ outliers, the galaxies follow the Tully-Fisher relation remarkably well, even in the presence of striking tidal distortion. Although most of the outliers show signs of strong star formation during the last $\sim 100 - 300$ Myr, gasdynamical effects are probably the dominant cause of their anomalous Tully-Fisher properties. Strong effects from morphological distortion and/or dissipationless kinematic distortion are rare.

Four outliers with small emission line widths have very centrally concentrated emission and truncated rotation curves. Recent gas infall after a close galaxy-galaxy pass or a minor merger can trigger this emission and can enhance the bulges of spiral galaxies. These four galaxies may be local counterparts to the compact, blue galaxies observed at intermediate redshift, including the compact narrow emission line galaxies.

The remaining galaxies have only a small zero-point offset from the Courteau (1997) TF relation for more isolated galaxies, but the pairs have a shallower slope (2.6σ significance) and a 25% larger scatter. We argue that triggered star formation is one significant contributor to the slope difference. We characterize the non-outlier sample with measures of distortion and star formation to search for third parameter dependence in the residuals of the TF relation. Severe kinematic distortion is the only significant predictor of TF residuals, although this distortion is not responsible for the slope difference.

Our results have several implications for TF studies at moderate or high redshift:

1. Morphological distortion alone rarely results in strong effects on the TF properties of galaxies. Gasdynamical effects on the rotation curve are much more common. These effects together give rise to a small set of outliers ($\sim 10\%$ of our sample).
2. Outliers due to interaction-induced distortion are easily removed by sigma clipping. This clipping provides a method for identifying galaxies with concentrated emission in an epoch of bulge enhancement, such as the compact, narrow emission line galaxies.
3. Luminous galaxies require prohibitively large bursts of star formation to move off the TF relation; at least locally, bursts of star formation will affect only low-mass galaxies. Therefore, the slope of the TF relation, while difficult to measure, is at least as fundamental for quantifying luminosity evolution as the zero-point offset.

We conclude that detection of moderate ($\gtrsim 0.5$ magnitudes in rest-frame R) luminosity evolution should be possible with high-redshift samples the size of this 90-galaxy study, even in the presence of some tidal distortion.

We thank Norman Grogin for the use of his additions to the GALPHOT package, and for other software and useful suggestions. We thank Sheila Kannappan for insightful comments on linewidth measurement techniques, Daniel Koranyi and Jan Kleyna for useful comments and software relating to galaxy coordinate systems and photometric calibrations, and Jeffrey Sutherland for helping to analyze the simulations. This research is supported in part by the Smithsonian Institution. We are grateful to the Caltech Center for Advanced Computing Research and NASA Offices of Space Sciences, Aeronautics, and Mission to Planet Earth for providing computing resources.

REFERENCES

Abraham, R. G., Valdes, F., Yee, H. K. C., & van den Bergh, S. 1994, *ApJ*, 432, 75

Barton, E. J., Bromley, B. C., & Geller, M. J. 1999, *ApJ*, 511, L25

Barton, E. J., Geller, M. J., & Kenyon, S. J. 2000a, *ApJ*, 530, 660, BGK

Barton, E. J., Geller, M. J., & Kenyon, S. J. 2000b, in preparation

Barton, E. J., Kannappan, S. J., Kurtz, M. J., & Geller, M. J. 2000c, *PASP*, 112, 367

Barton, E. J., & van Zee, L. 2000, in preparation

Beauvais, C., & Bothun, G. 1999, *ApJS*, 125, 99

Bershady, M. A., Jangren, A., & Conselice, C. J. 2000, *AJ*, 119, 2645

Bershady, M. A., & Andersen, D. R. 2000, in *Dynamics of Galaxies: from the Early Universe to the Present*, eds. F. Combes, G. A. Mamon, and V. Charmandaris, (ASP, Vol. 197), p. 175

Bureau, M., Mould, J. R., & Staveley-Smith, L. 1996, *ApJ*, 463, 60

Cole, S., Aragon-Salamanca, A., Frenk, C. S., Navarro, J. F., & Zepf, S. E. 1994, *MNRAS*, 271, 781

Conselice, C. J., Bershady, M. A., & Jangren, A. 2000, *ApJ*, 529, 886

Conselice, C. J., Bershady, M. A., & Gallagher, J. S., III 2000, *A&A*, 354, 21

Courteau, S. 1996, *ApJS*, 103, 363

Courteau, S. 1997, *AJ*, 114, 2402, C97

Courteau, S., & Rix, H.-W. 1999, *ApJ*, 513, 561

Dale, D. A., Giovanelli, R., Haynes, M. P., Scodéglio, M., Hardy, E., & Campusano, L. E. 1997, *AJ*, 114, 455

Dale, D. A., Giovanelli, R., Haynes, M. P., Hardy, E., & Campusano, L. E. 1999, *AJ*, 118, 1468

Eisenstein, D. J., & Loeb, A. 1996, *ApJ*, 459, 432

Franx, M., & de Zeeuw, T. 1992, *ApJ*, 392, L47

Frei, Z. & Gunn J. E. 1994, *AJ*, 108, 1476

Giovanelli, R., et al. 1997a, *AJ*, 113, 22

Giovanelli, R., et al. 1997b, *AJ*, 113, 53

Giovanelli, R., Haynes, M. P., da Costa, L. N., Freudling, W., Salzer, J. J., & Wegner, G. 1997c, *AJ*, 114, 455

Grogin, N. A., & Geller, M. J. 1999, *AJ*, 118, 2561

Guzmán, R., et al. 1996, *ApJ*, 460, L5

Guzmán, R., et al. 1997, *ApJ*, 489, 559

Haynes, M. P., et al. 1999a, AJ, 117, 1668
Haynes, M. P., et al. 1999b, AJ, 117, 2039
Jørgensen, I. 1994, PASP, 106, 967
Kauffmann, G., & White, S. D. M. 1993, MNRAS, 261, 921
Kobulnicky, H. A., & Zaritsky, D. 1999, ApJ, 511, 118
Kolatt, T. S., et al. 1999, ApJ, 527, 199
Koo, D. C., Bershady, M. A., Wirth, G. D., Stanford, S. A., & Majewski, S. R. 1994, ApJ, 427, L9
Koo, D. C., Guzmán, R., Faber, S. M., Illingworth, G. D., & Bershady, M. A. 1995, ApJ, 440, L49
Kuijken, K., & Dubinski, J. 1995, MNRAS, 277, 1341
Landolt, A. U. 1992, AJ, 104, 340
Matthews, L. D., van Driel, W., Gallagher, J. S., III 1998, AJ, 116, 2196
McGaugh, S. S., Schombert, J. M., Bothun, G. D., & de Blok, W. J. G. 2000, ApJ, 533, 99
Mihos, J. C., & Hernquist, L. 1994, ApJ, 425, 13
Mihos, J. C., & Hernquist, L. 1996, ApJ, 464, 641
Mo, H. J., & Mao, S. 2000, MNRAS, in press
Mould, J., Han, M., & Bothun, G. 1989, ApJ, 347, 112
Navarro, J. F., & Steinmetz M. 2000, ApJ, 538, 477
Neinstein, E., Maoz, D., Rix, H.-W., & Tonry, J. L. 1999, AJ, 117, 2666
Odewahn, S. C., Windhorst, R. A., Driver, S. P., & Keel, W. C. 1996, ApJ, 472, 13
O’Neil, K., Bothun, G. D., & Schombert, J. 2000, AJ, 119, 136
Pierce, M. J., & Tully, R. B. 1992, ApJ, 387, 47, PT92
Phillips, A. C., et al. 1997, ApJ, 489, 543
Rubin, V. C., Burstein, D., Ford, W. K., Jr., & Thonnard, N. 1985, ApJ, 289, 81
Rudnick, G., Rix, H.-W., & Kennicutt, R. C., Jr. 2000, ApJ, 538, 569
Simard, L., & Pritchett, C. J. 1998, ApJ, 505, 96
Somerville, R. S., & Primack, J. R. 1999, MNRAS, 310, 1087
Spayberry, D., Bernstein, G. M., Impey, C. D., & Bothun, G. D. 1995, ApJ, 438, 72
Tully, R. B., & Fisher, J. R. 1977, A&A, 54, 661
Tully, R. B., & Fouqué, P. 1985, 58, 67
Tully, R. B., & Pierce, M. J. 2000, ApJ, 533, 744, TP00
van den Bergh, S., Abraham, R. G., Ellis, R. S., Tanvir, N. R., Santiago, Basilio, X., & Glazebrook, K. G. 1996, AJ, 112, 359

Verheijen, M. A. W. 1997, Ph.D. Thesis, U. Groningen

Vogt, N. P., et al. 1996, ApJ, 465, L15

Vogt, N. P., et al. 1997, ApJ, 479, L121

Windhorst, R., Odewahn, S., Burg, C., Cohen, S., & Waddington, I. 1999, Ap&SS, 269, 243

Willick, J. A. 1994, ApJS, 92, 1

Willick, J. A., Courteau, S., Faber, S. M., Burstein, D., & Dekel, A. 1995, ApJ, 446, 12

Willick, J. A., Courteau, S., Faber, S. M., Burstein, D., Dekel, A., & Kolatt, T. 1996, ApJ, 457, 460

Zaritsky, D., & Rix, H.-W. 1997, ApJ, 477, 118

Zwicky, F., Herzog, E., Wild., P., Karpowicz, M., & Kowal, C. 1961-1968, Catalogue of Galaxies and of Clusters of Galaxies (Pasadena: California Institute of Technology)

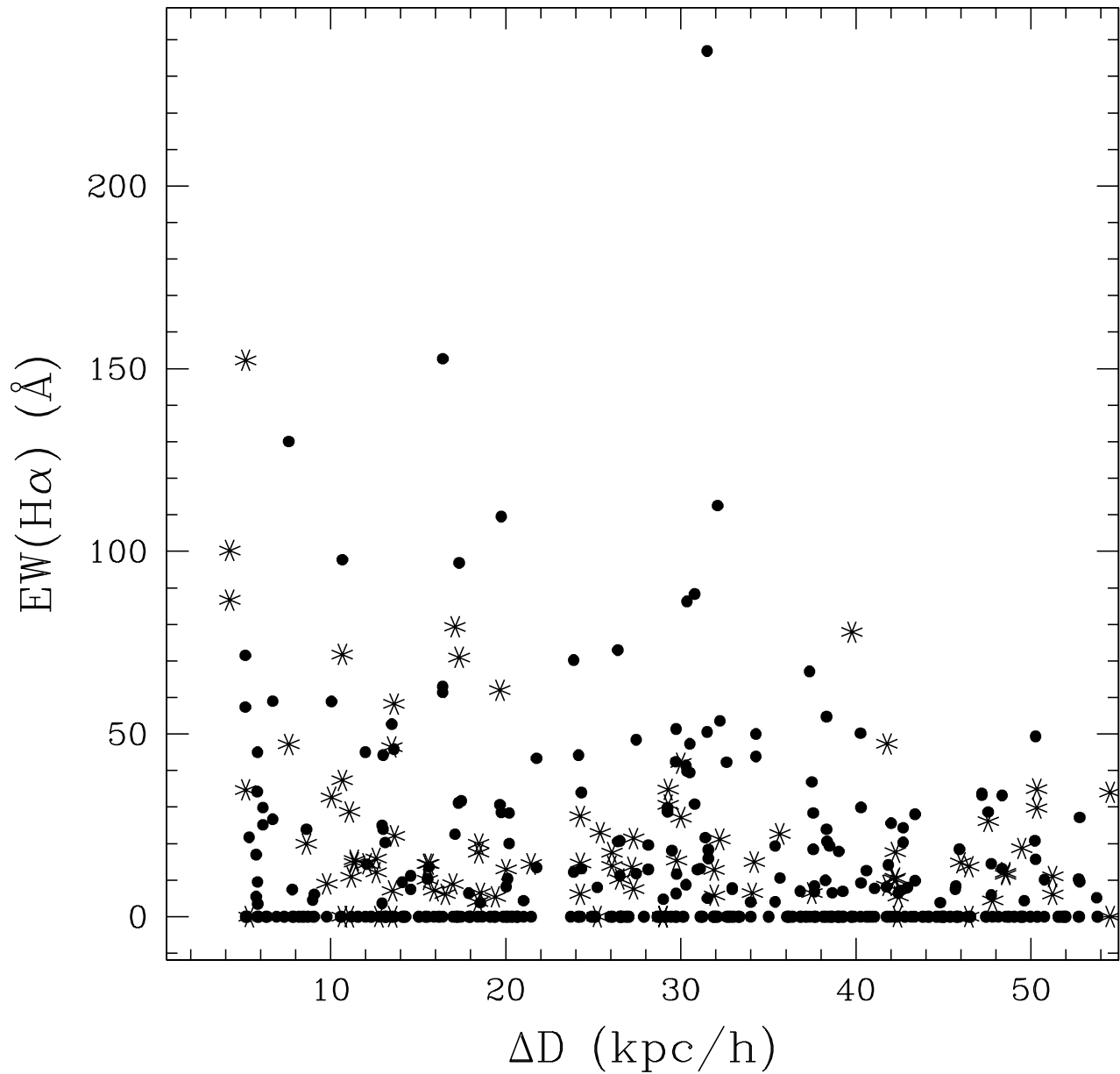


Fig. 1.— Nuclear EW(H α) as a function of ΔD from Fig. 2 of Barton, Geller, & Kenyon (2000). The stars denote the galaxies in this study.

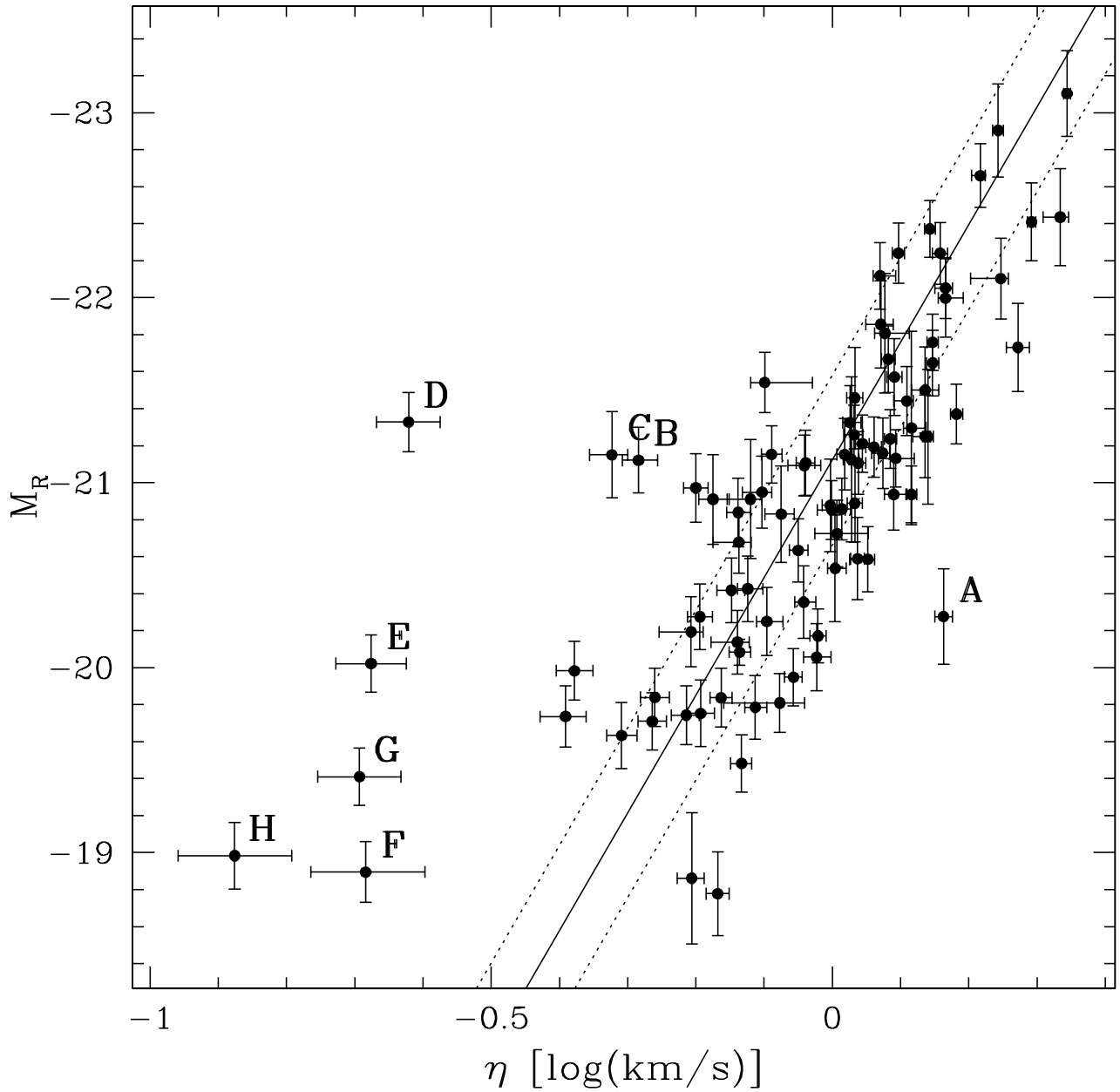


Fig. 2.— The TF distribution for galaxies in pairs, with parameters computed with the prescriptions of Courteau (1997). The solid line shows the C97 relation (shifted according to the relation $r - R = 0.354$); the dotted lines show the C97 1σ scatter.

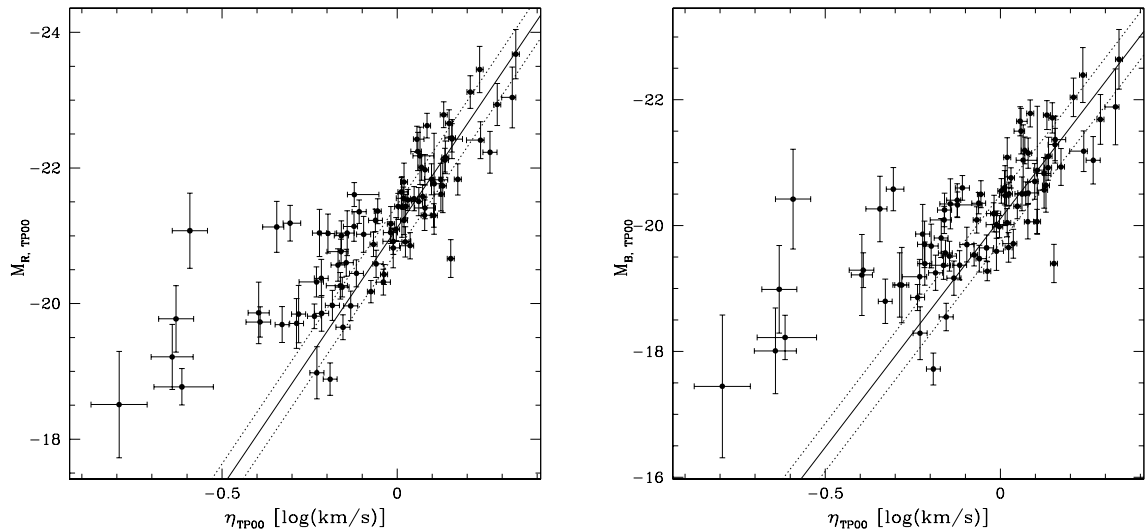


Fig. 3.— The TF relation adjusted to the prescriptions of Tully & Pierce (2000) in (a) R , and (b) B . In each panel, the solid line shows the TP00 relation; the dotted lines show the TP00 1σ scatter.

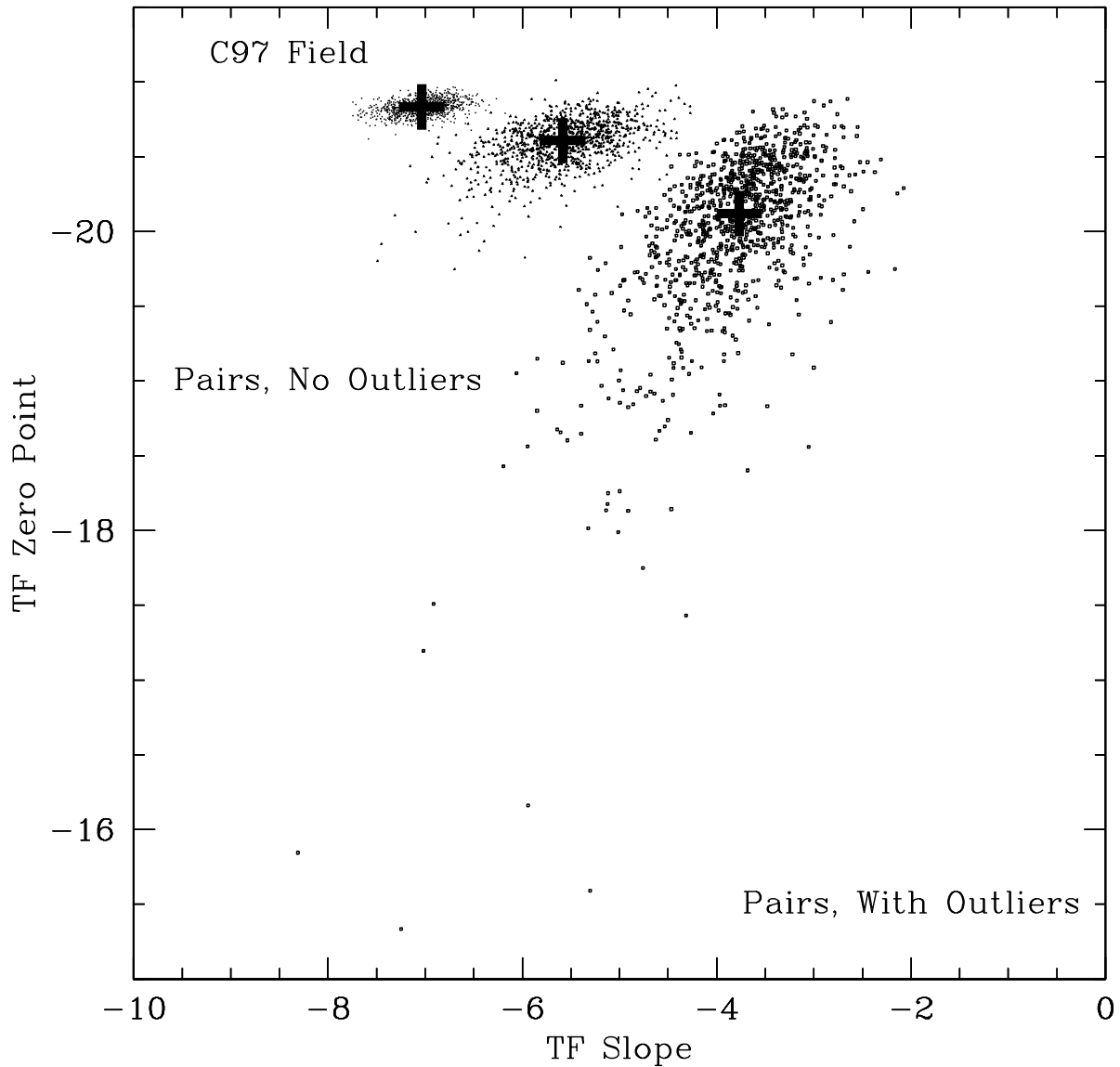


Fig. 4.— TF fits to full sample, our sample without the 8 outliers, and the C97 data (shifted via $r - R = 0.354$). The crosses are the solutions, the smaller points are the results from the Monte Carlo simulations, indicating the confidence intervals.

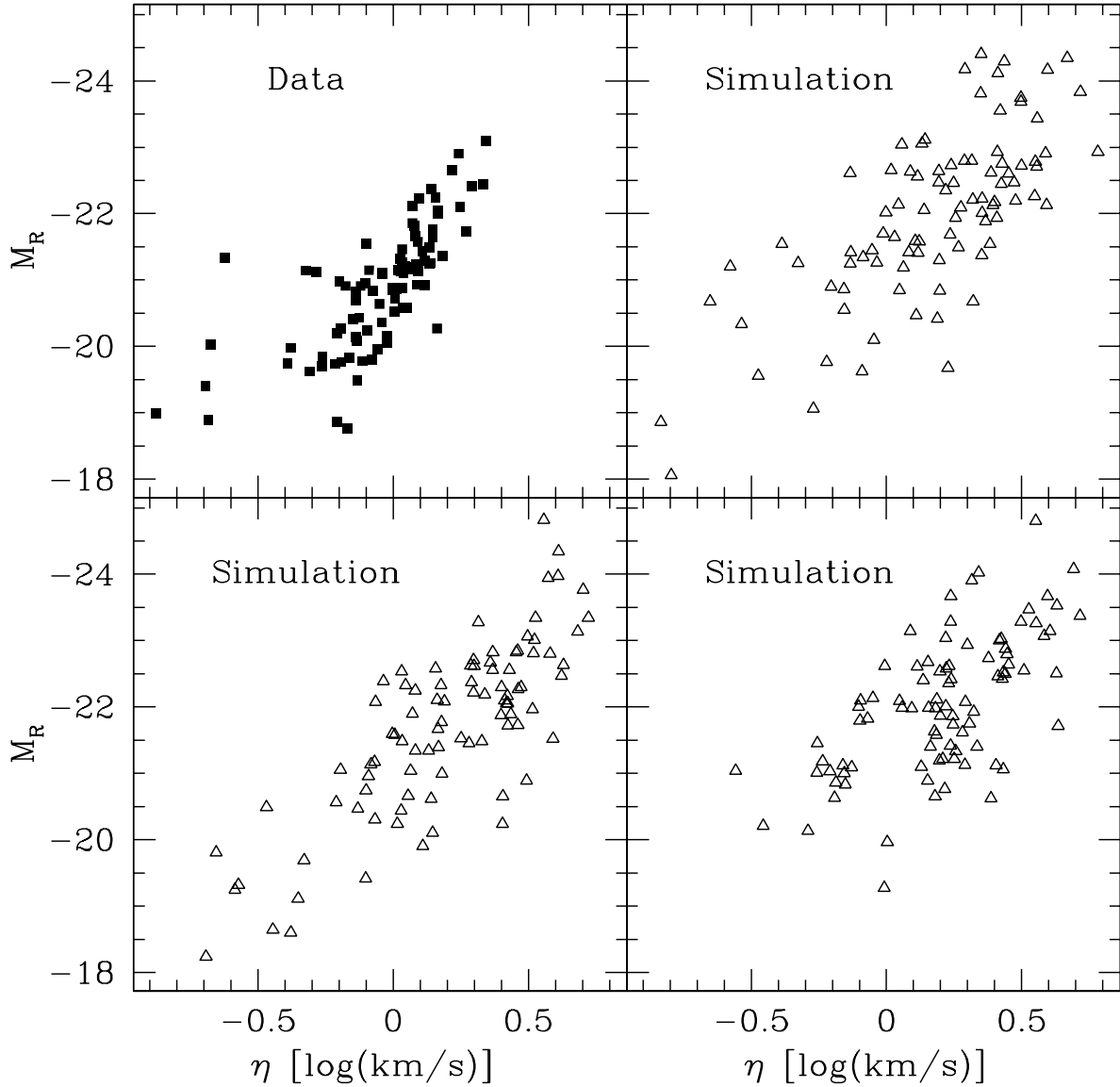


Fig. 5.— Comparison of the TF distribution of the pair data and three Monte Carlo realizations: (a) the full dataset, and (b) – (d) three realizations using the TF parameters and scatter from the full dataset. The distributions appear different from the data — the high-mass scatter in the data is much smaller than that of the simulations. Thus, we infer that the low-mass scatter is due to a non-Gaussian tail of outliers.

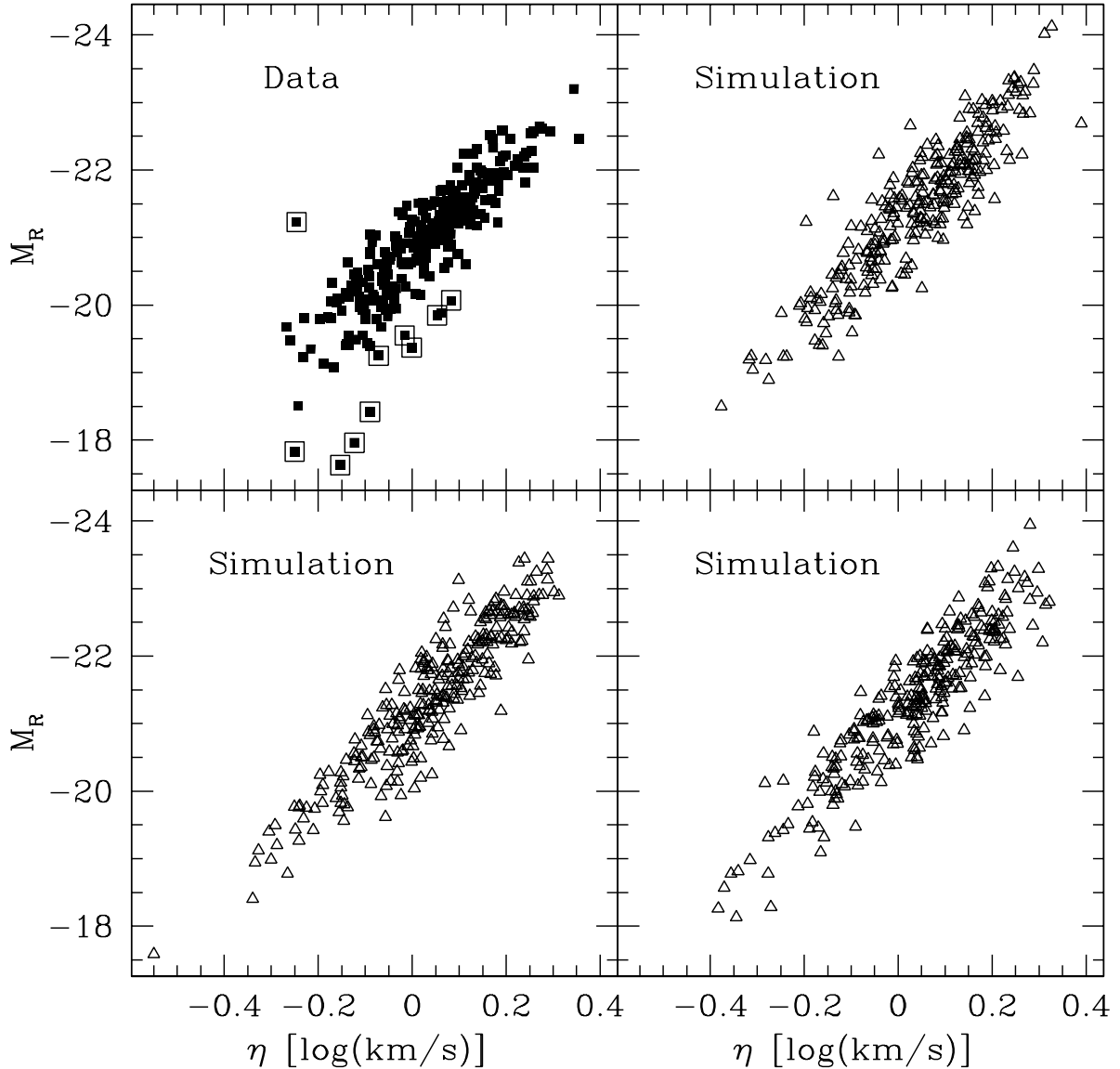


Fig. 6.— Comparison of the TF distribution of the C97 data and three Monte Carlo realizations: (a) the full dataset, with 3σ “outliers” marked, and (b) – (d) three realizations using the TF parameters and scatter from the data *with the outliers*. The Monte Carlo realizations are similar to the TF distribution of the data points; there is no evidence that the marked points are true, non-Gaussian outliers.

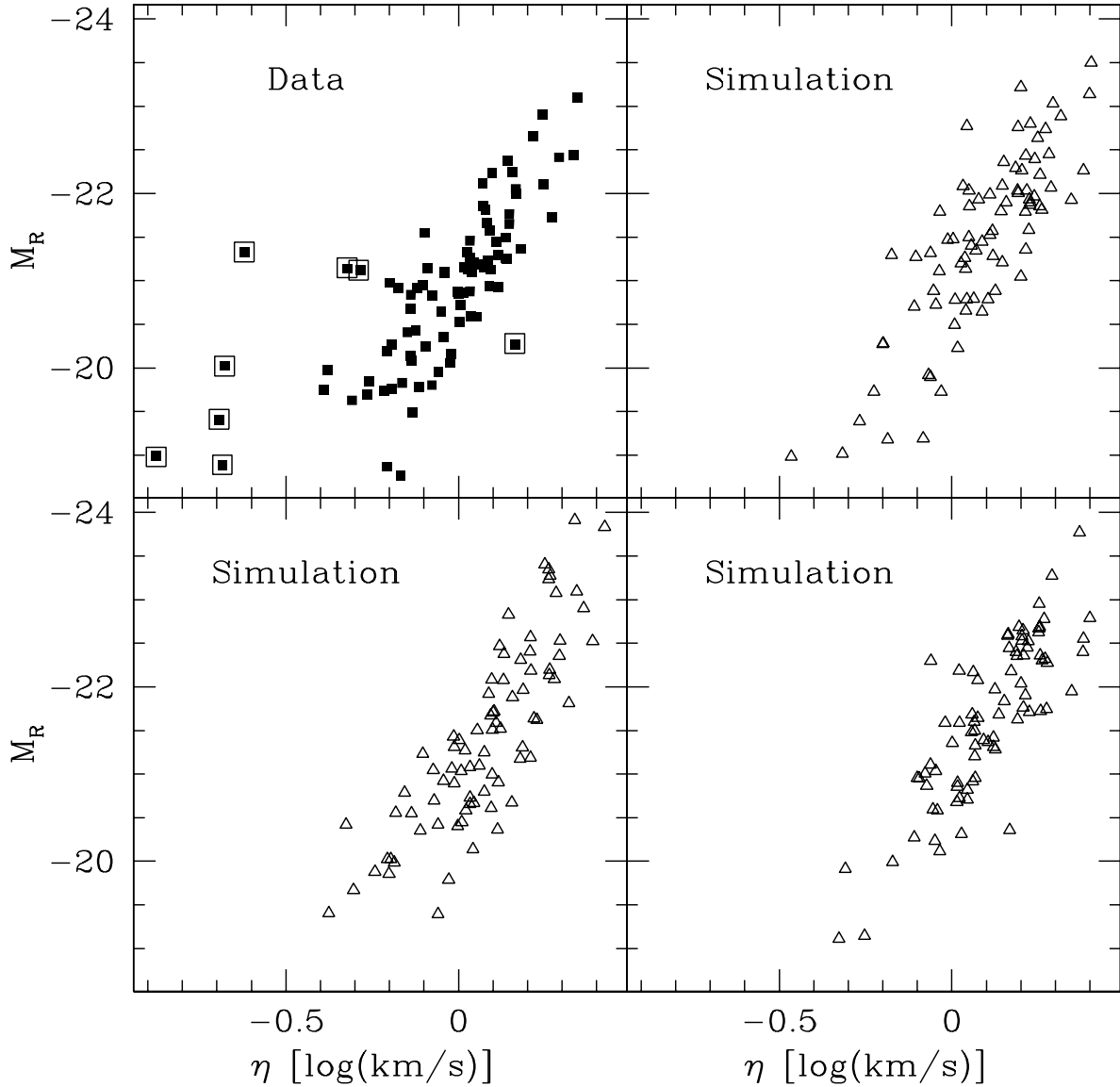


Fig. 7.— Comparison of the TF distribution of the pair data and three Monte Carlo realizations: (a) the full dataset, with outliers marked, and (b) – (d) three realizations using the TF parameters and scatter from the data without the outliers. The Monte Carlo realizations are similar to the TF distribution of the non-outlier data points.

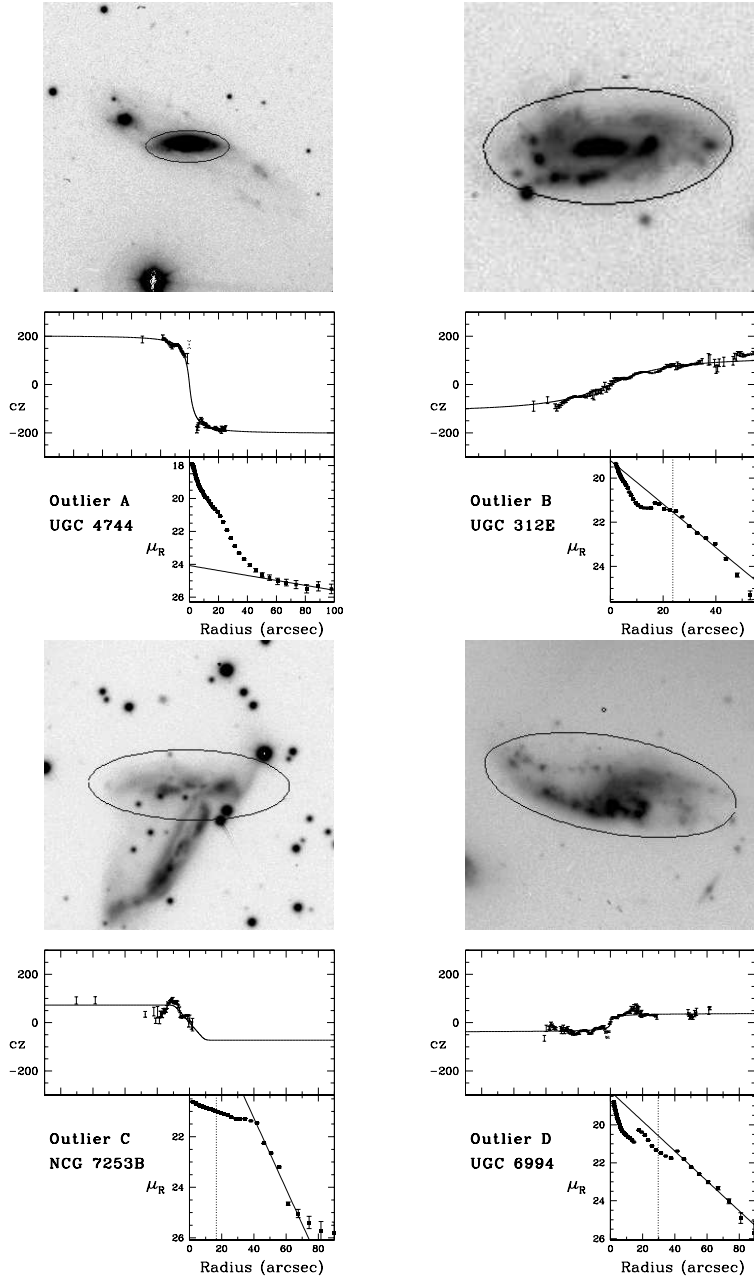


Fig. 8.— Outliers to the C97 TF relation. For each galaxy, the top panel is the *B*-band image, with the ellipse we use to measure ϵ . The middle panel is the rotation curve, on the same spatial scale as the image, and the bottom panel is the *R* surface brightness. The vertical line marks $2.15 R_{\text{disk}}$, the spatial position used to measure V_c .

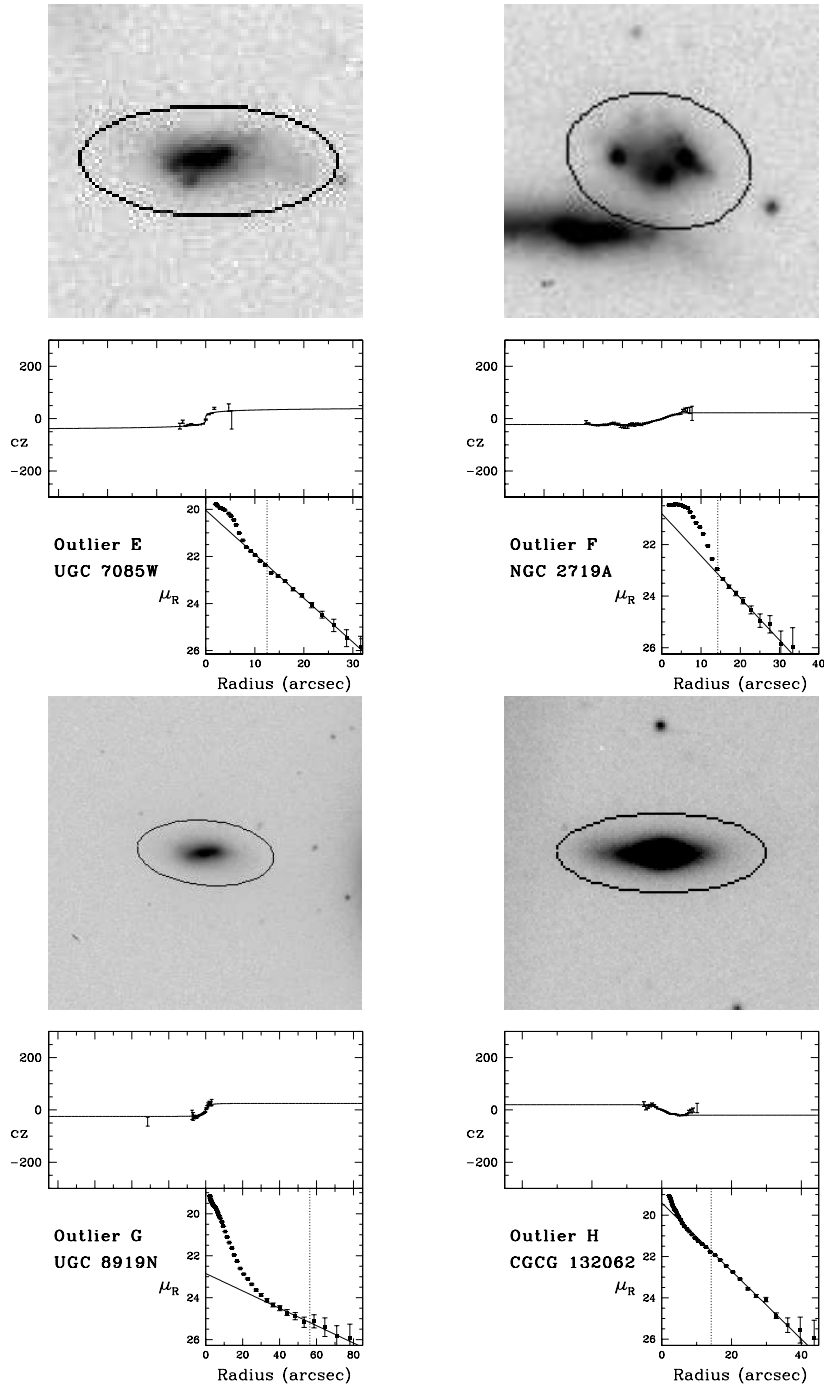


Fig. 9.— The low-mass outliers, “E” – “H” (see Fig. 8).



Fig. 10.— Simulation from Barton et al. 1999. We show a face-on “Milky Way B” model galaxy with an intermediate halo size and moderate impact parameter (see Barton et al. 1999), after a prograde encounter with an equal-mass galaxy.

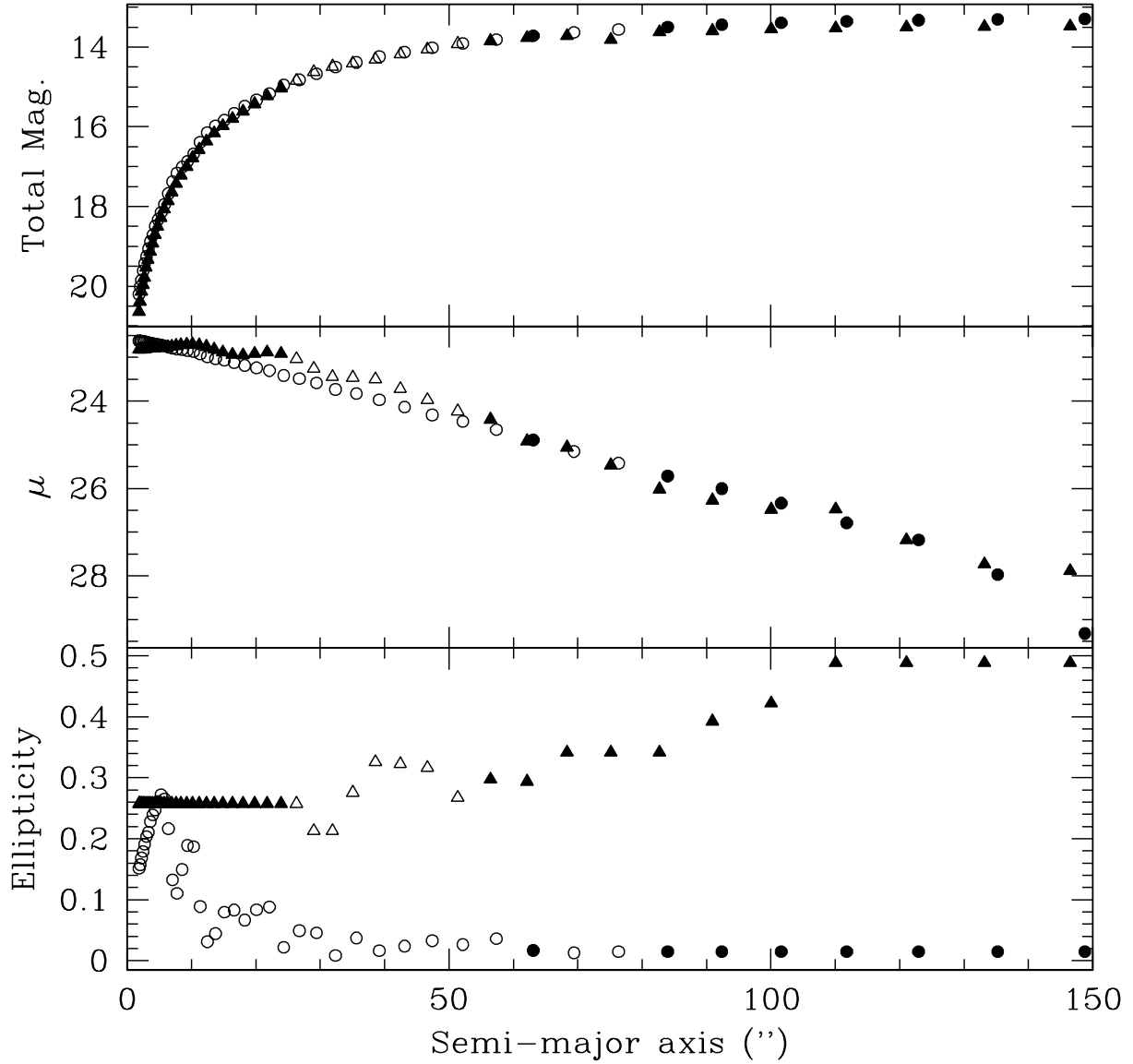


Fig. 11.— Results of the “photometry” on the simulated interaction (triangles) and the initial simulated galaxy (circles). Open points represent ellipses fit by the program; closed points were fixed by the program or represent non-convergent fits. The interaction has very little effect on the total magnitude and the surface brightness profile, but the ellipticity deviates from the “true” value of 0.

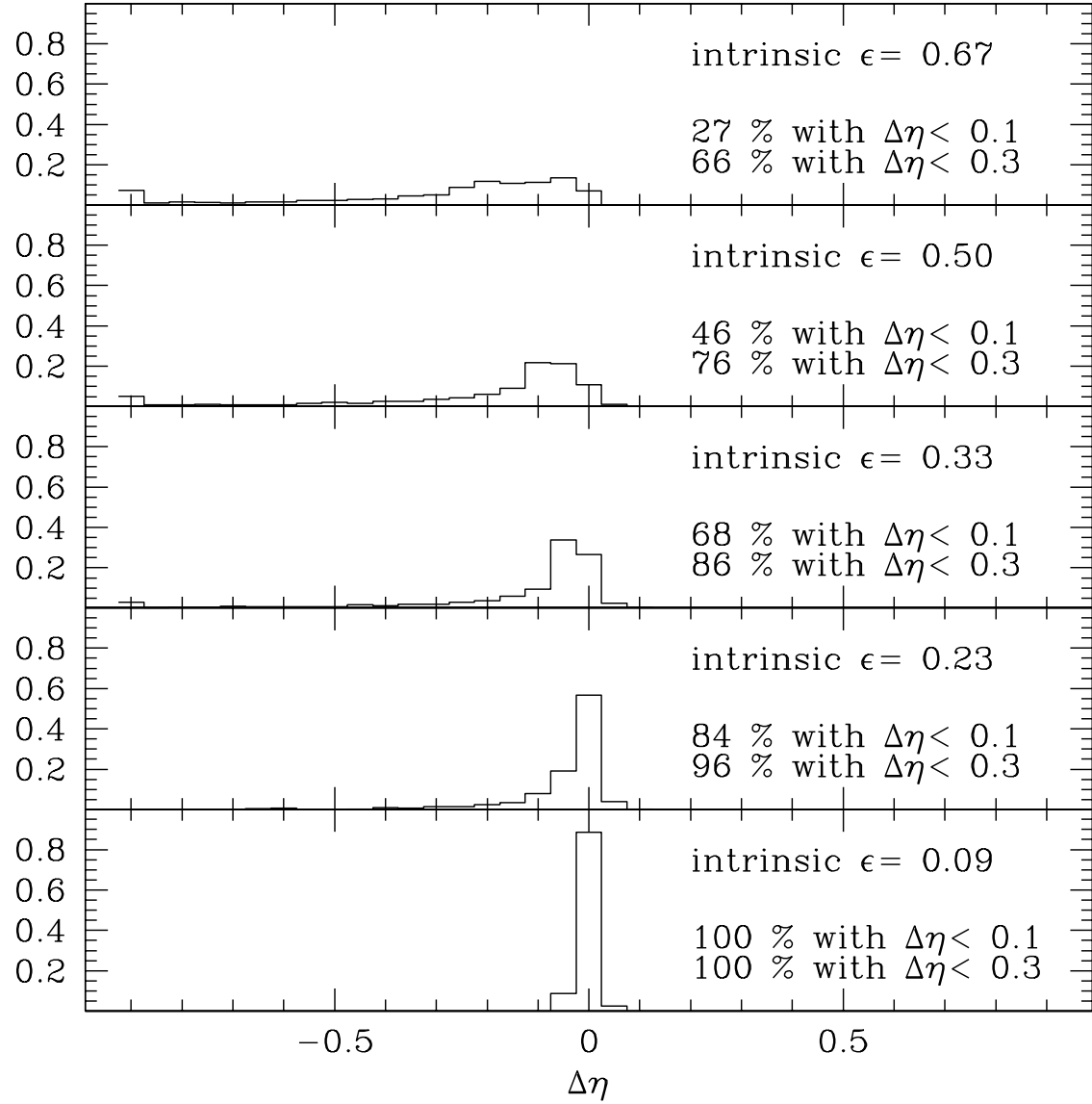


Fig. 12.— Effects of intrinsic elongation on the inferred velocity width parameter, for different values of the intrinsic ellipticity, ϵ . The histograms represent measurements from observation angles spaced uniformly about the unit circle; we include measurements only when $i_{\text{meas}} > 40^\circ$.

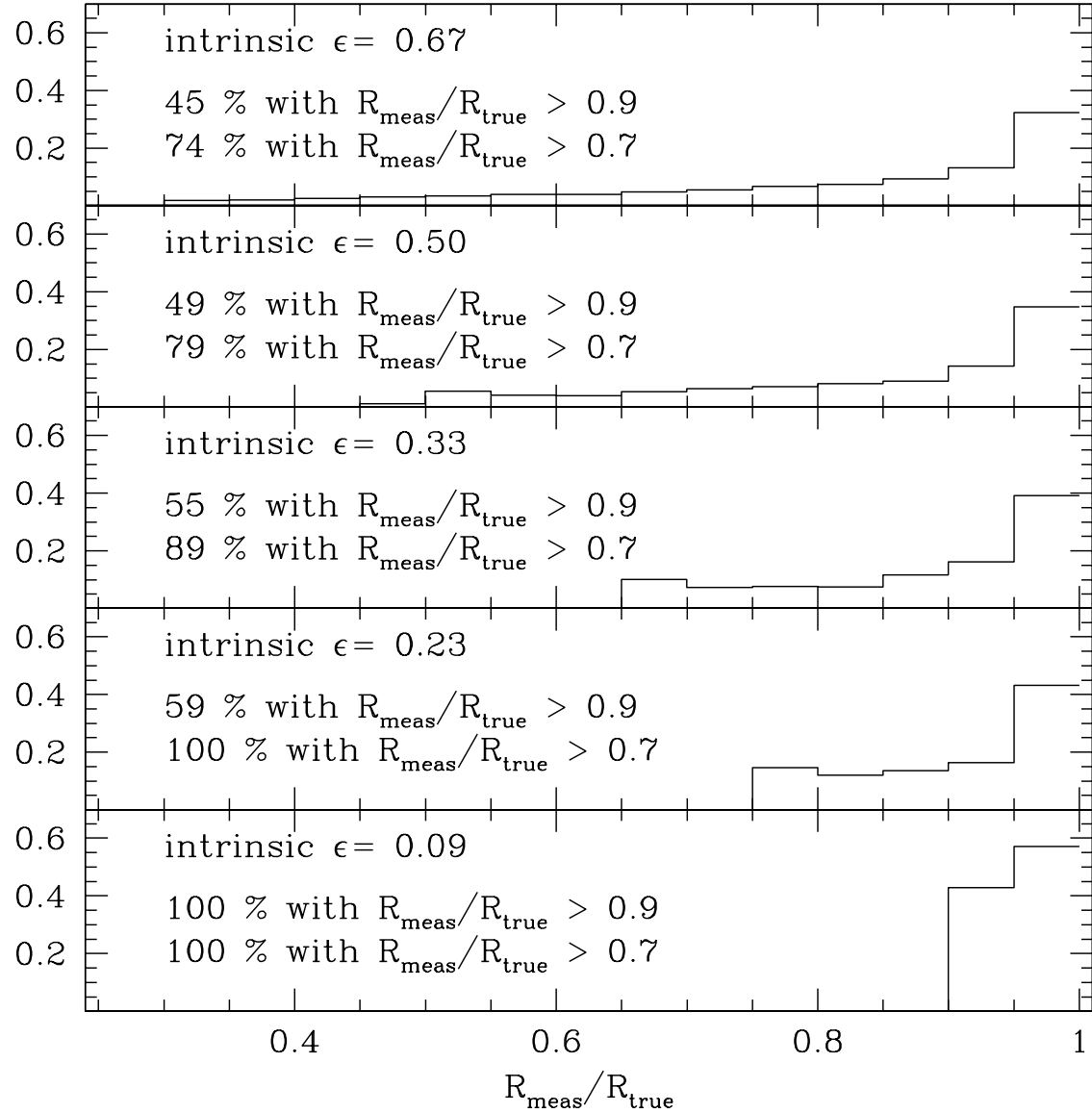


Fig. 13.— Effects of intrinsic elongation on the measured major axis length, R_{meas} . As in Fig. 12, we “observe” ellipses from points spaced uniformly around the unit circle, and restrict the sample to measured inclinations $i_{\text{meas}} < 40^\circ$.

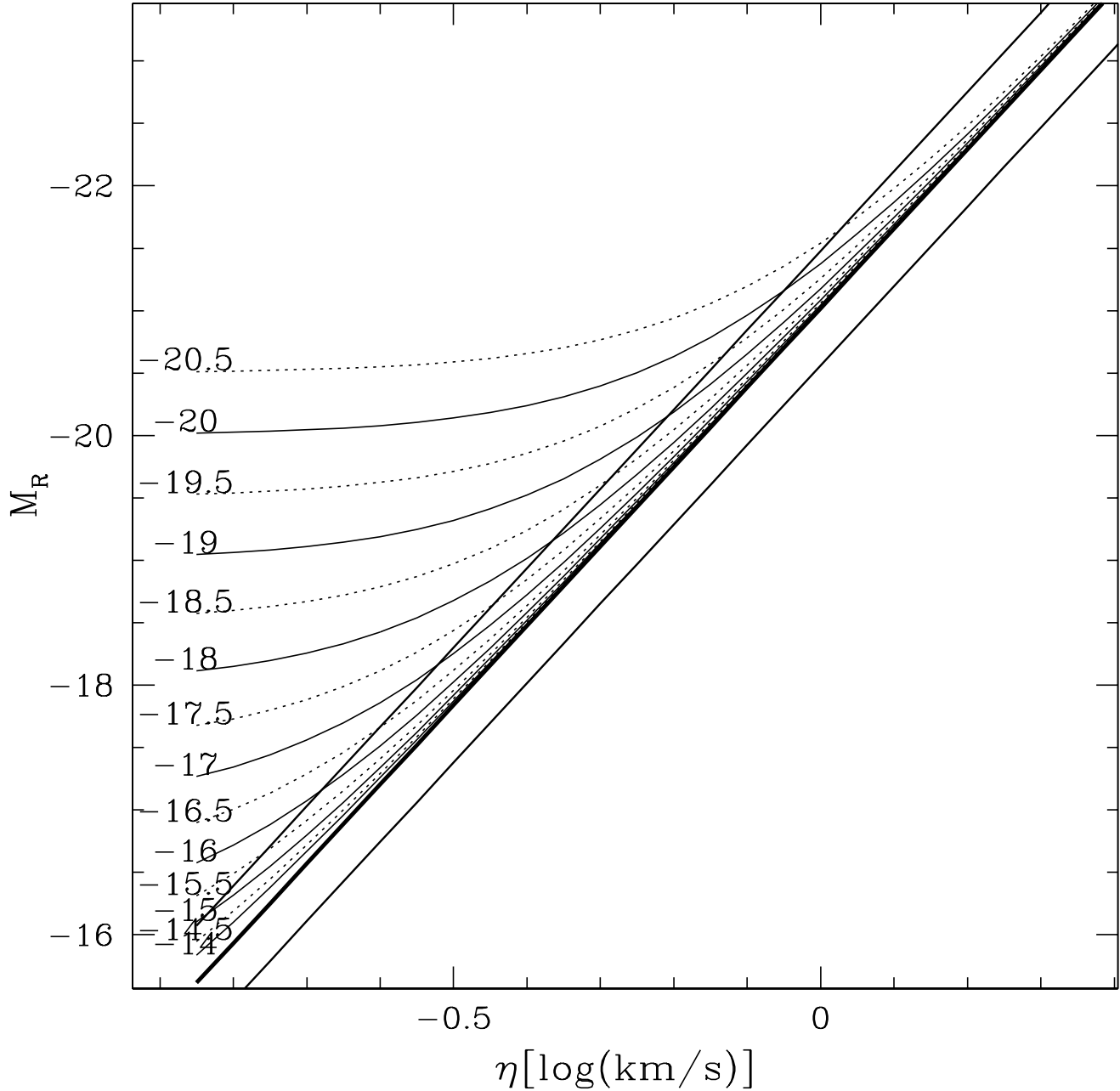


Fig. 14.— The luminosity effects of added starbursts: we plot the shift the TF properties from a burst of absolute magnitude M , assuming the only effect of the burst is luminosity evolution. We label the contours with M , in magnitudes. Because the TF relation measures fractional deviations, a burst of constant strength changes the slope of the TF relation.

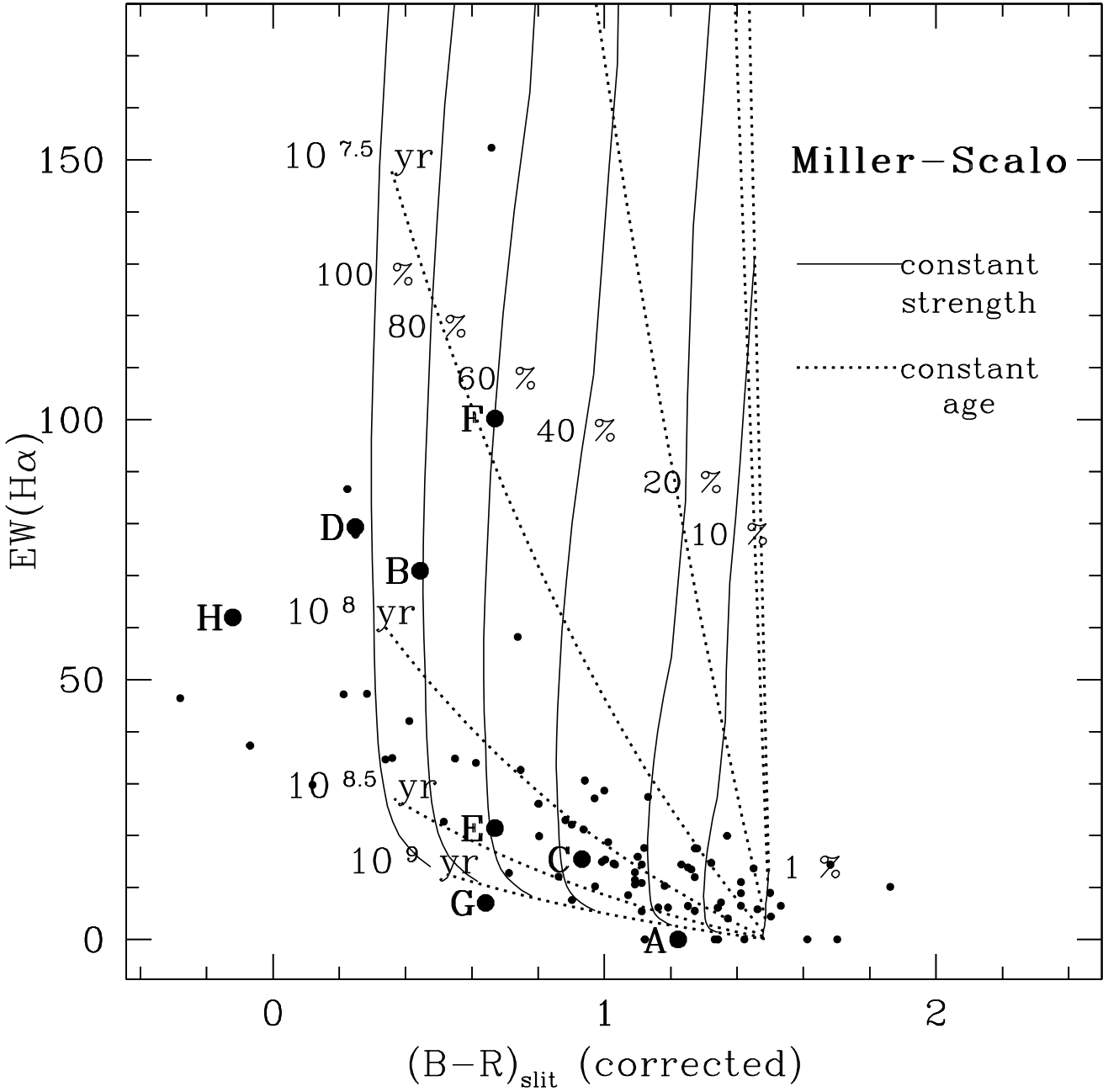


Fig. 15.— Central bursts of star formation in the centers of the pair galaxies, with the TF outliers labeled. We plot $B - R$ colors in the central (spectroscopic) aperture vs. H α equivalent widths. We correct the colors for reddening based on the Balmer decrement. The contours are lines of constant R -band burst strength (solid) and age (dotted), computed with the Leitherer et al. (1999) models, assuming a constant star formation rate over time, a Miller-Scalo IMF with solar metallicity, and $B - R = 1.5$ for the population present before the interaction (see Barton et al. 2000b).

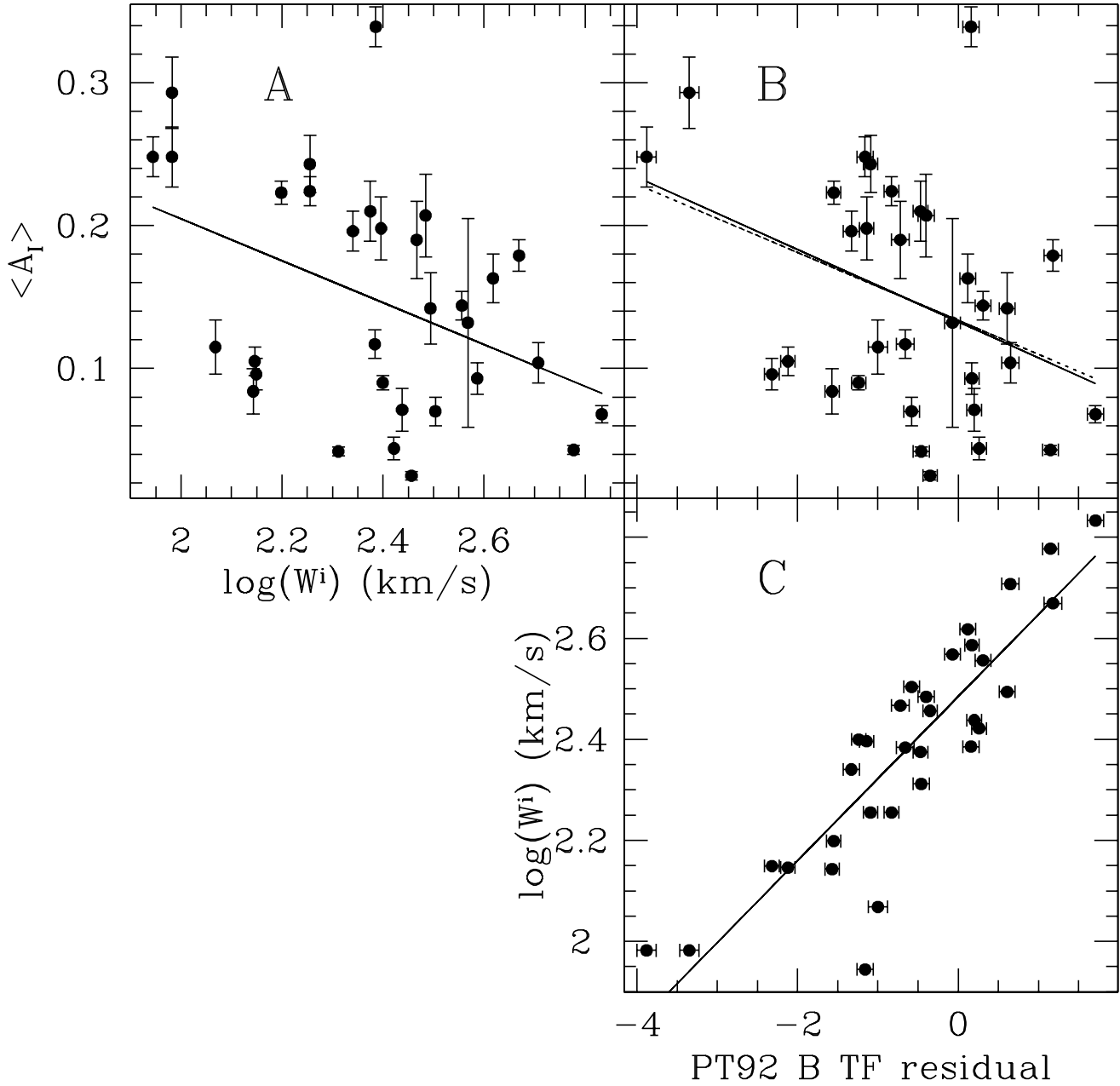


Fig. 16.— Systematic effects on TF residuals in the Zaritsky & Rix (1997) data. The figure shows that the correlation in Panel B (between TF residual and galaxy asymmetry) results from the more fundamental correlation between linewidth, W^i , and asymmetry, in panel A, and the systematic error in the Pierce & Tully (1992) TF relation, shown as a tight correlation between the residual and W^i in panel C.

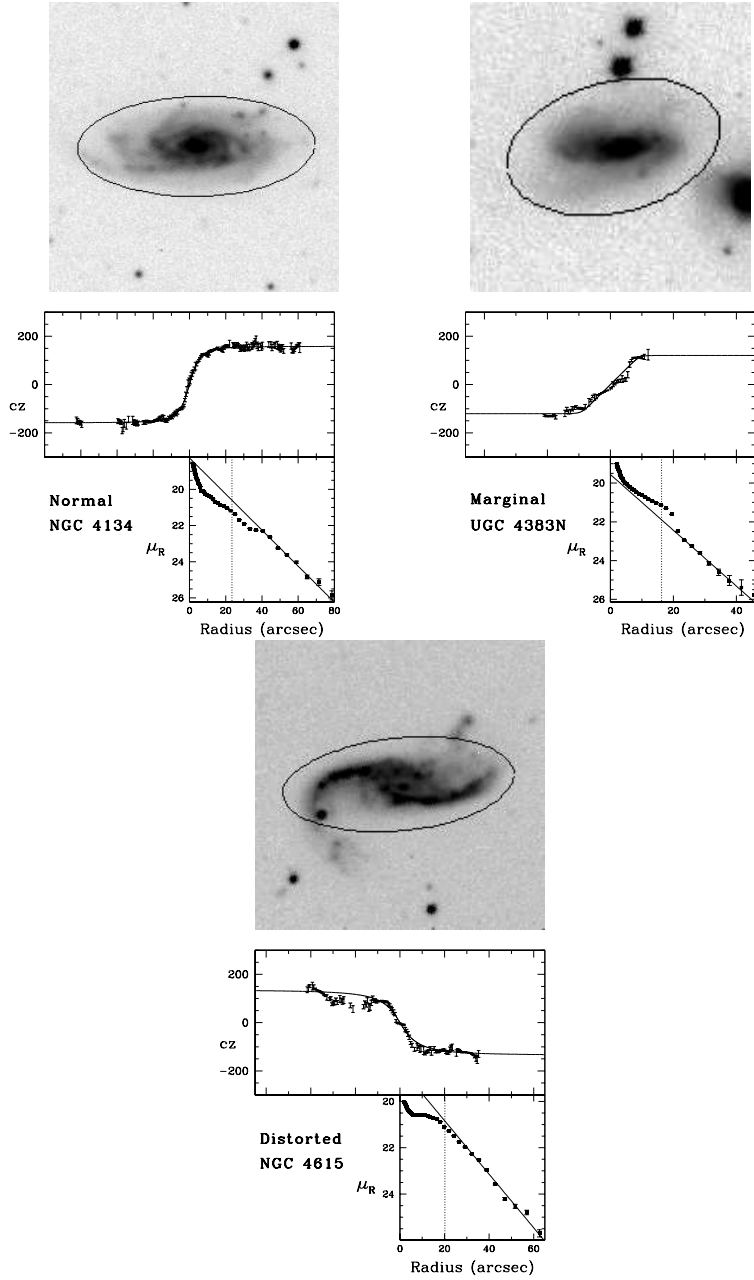


Fig. 17.— Examples of galaxies with “normal”, “marginal”, and “distorted” rotation curves. For each galaxy, the top panel is the B -band image, with the ellipse we use to measure ϵ . The middle panel is the rotation curve, on the same spatial scale as the image, and the bottom panel is the R surface brightness. The vertical line marks $2.15 R_{\text{disk}}$, the spatial position used to measure V_c .

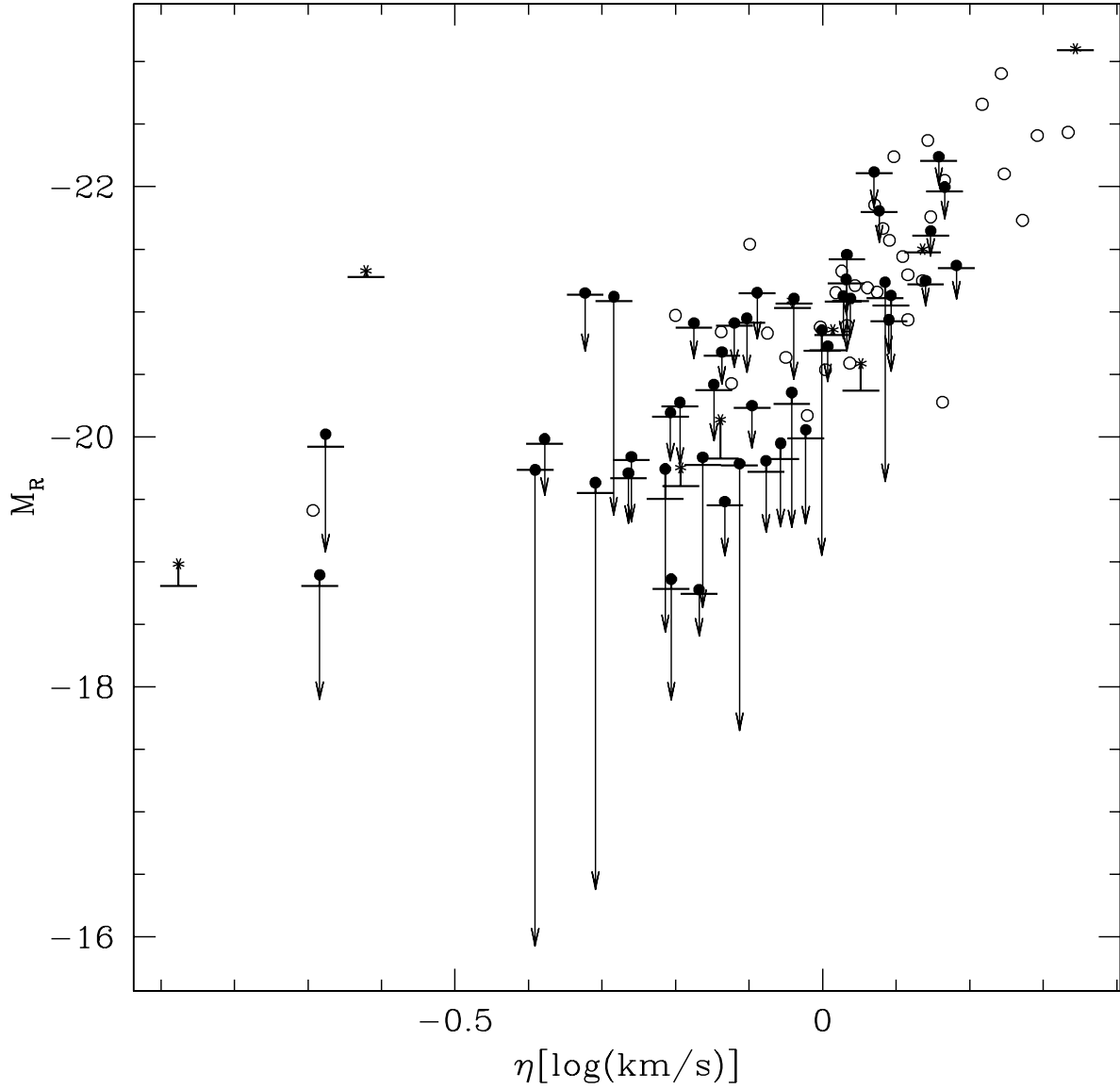


Fig. 18.— The possible effects of triggered star formation. We plot the TF relation for the 89 pair galaxies with nuclear spectra. Assuming the Miller-Scalo IMF with solar metallicity, a constant star formation rate, and an old population with $B - R = 1.5$, we plot galaxies with $0 < s_R < 1$ as filled circles, galaxies with $s_R = 1$ as stars, and galaxies with little central star formation (hence no valid solution for s_R) as open circles, where s_R is the new R burst strength in the aperture of the nuclear spectrum. For galaxies with $s_R > 0$, the horizontal line shows the lower-limit correction for the central burst only (i.e., the magnitude with burst removed). For galaxies with $0 < s_R < 1$, the arrow shows the upper-limit correction, assuming s_R is constant throughout. Starred galaxies (with $s_R = 1$) have no measured upper limit for the correction. Note the change in y-axis scale from Fig. 2.

Table 1. TF Parameters

Parameter	Description
m_R	total R magnitude
m_B	total B magnitude
ϵ	disk ellipticity
R_{disk}	radial disk scale length
m	slit misalignment angle (in the plane of the sky)
$V_{2.2}$	velocity width at $2.15 \times R_{\text{disk}}$ (C97)

Table 2. TF Properties

Reference Distribution	N_{gal}	All Curves		R -Band Outliers Removed		
		Δ_{TF} (mag.)	Scatter (mag.)	N_{gal}	Δ_{TF} (mag.)	Scatter (mag.)
Courteau (1997) r	90	-0.06 ± 0.10	1.00	82	0.14 ± 0.06	0.55
Tully & Pierce (2000) R	89	-0.46 ± 0.11	1.01	81	-0.26 ± 0.07	0.60
Tully & Pierce (2000) B	89	-0.50 ± 0.11	1.04	81	-0.30 ± 0.07	0.66
Pierce & Tully (1992) R	90	-0.87 ± 0.13	1.26	82	-0.61 ± 0.08	0.75
Pierce & Tully (1992) B	90	-0.75 ± 0.14	1.28	82	-0.50 ± 0.09	0.81

Note. — TF Statistics: (1) Reference distribution, (2) number of galaxies in the sample, (3) offset from the reference distribution, based on a fit of the TF relation with the slope fixed by the reference distribution; a negative offset indicates that the galaxies appear *overluminous* with respect to the reference distribution, and (4) scatter from the fit in (3). One galaxy is missing from the TP00 fits due to the different prescription for computing the inclination angle. (5) – (7) are the same as (2) – (4), for the distributions without the 8 R -band outliers.

Table 3. Relations Between m_{Zw} and the TF Parameters

Data	N_{gal}	a (mag.)	b (mag./dex)	c (mag./mag.)	$\sigma_{m,\text{Zw}}$ (mag.)
C97 “field” Sample	279	-1.370	1.711	1.187	0.421
Pairs	90	0.797	1.114	1.070	0.546

Note. — Fits to the relation $m_{\text{Zw}} = a + b\eta + cm$, where m_{Zw} is the Zwicky magnitude, η is the velocity width parameter, and m is the apparent magnitude (R -band for the pairs data, Gunn r for the C97 data), using the method of Willick (1994): (1) data set, (2) number of points, (3) – (5) results, (6) scatter.

Table 4. TF Relations

Data	N_{gal}	Δ_{TF} (mag.)	α_{TF} (mag./dex)	σ_{TF} (mag.)
C97 Sample	279	-20.83 ± 0.05	-7.03 ± 0.26	0.45 ± 0.03
Pairs	90	-20.12 ± 0.40	-3.77 ± 0.55	0.94 ± 0.15
Pairs, no outliers	82	-20.61 ± 0.15	-5.58 ± 0.50	0.56 ± 0.07

Note. — Fits to the TF relation $M_R = \Delta_{\text{TF}} + \alpha_{\text{TF}}\eta$, where η is the velocity width parameter, and M is the magnitude (R -band for the pairs data, converted to R from Gunn r for the C97 data): (1) data set, (2) number of points, (3) – (4) results, (5) scatter. The errors are the 68.3% confidence levels from the Monte Carlo simulation for the individual, not joint, parameters (e.g., 68.3% of all the simulations for the C97 sample had a computed offset within -20.83 ± 0.05).

Table 5. Outlier Properties

Galaxy/Label		z_{LG}	η	M_R	M_B	EW(H α) (Å)	EW(H δ) (Å)	$B - R$	$R_{e,R}$ (h $^{-1}$ kpc)	$R_{e,B}$ (h $^{-1}$ kpc)
UGC 4744	A	0.0078	0.16	-20.27	-18.83	0.0 ± 1.0	-1.3 ± 0.3	1.44	1.8	1.8
UGC 312E	B	0.0152	-0.28	-21.12	-20.53	71.0 ± 1.4	0.8 ± 0.8	0.59	5.2	5.5
NGC 7253B	C	0.0162	-0.32	-21.14	-20.14	15.4 ± 1.2	0.0 ± 0.7	1.00	10.4	10.6
UGC 6944	D	0.0111	-0.62	-21.33	-20.68	79.3 ± 1.6	0.0 ± 0.3	0.65	5.0	5.0
UGC 7085W	E	0.0210	-0.68	-20.03	-19.30	21.4 ± 1.4	-3.8 ± 0.3	0.74	2.3	2.1
NGC 2719A	F	0.0103	-0.68	-18.89	-18.47	100.2 ± 3.0	4.2 ± 0.3	0.42	1.2	1.2
UGC 8919N	G	0.0095	-0.69	-19.40	-18.31	7.1 ± 1.0	-3.9 ± 0.3	1.09	1.9	1.8
CGCG 132-062	H	0.0094	-0.88	-18.99	-18.02	62.0 ± 1.1	0.0 ± 0.1	0.97	1.2	1.0

Note. — Properties of the TF Outliers: (1) Name, (2) label for Fig. 2, (3) redshift, corrected for motion in the local group, (4) velocity width parameter, (5) M_R (corrected for extinction with the C97 prescriptions), (6) M_B (corrected), (7) equivalent width of H α , (8) equivalent width of H δ (a negative value denotes absorption), (9) $B - R$, (10) R half-light radius, and (11) B half-light radius.

Table 6. More Outlier Properties

Galaxy	sr	$M_{R,\text{burst,slit}}$ (mag.)	f_{slit}	Expected residual (mag.)	TF residual (mag.)	Comment
UGC 4744	—	—	—	—	+1.89	ambiguous
UGC 312E	0.80	-17.3	3.8%	-0.16	-1.81	ambiguous
NGC 7253B	0.35	-16.4	3.7%	-0.09	-2.07	poorly-sampled curve
UGC 6944	1.00	-17.9	4.3%	-1.17	-4.16	tidal elongation
UGC 7085W	0.58	-17.4	15.5%	-1.08	-3.21	truncated curve
NGC 2719A	0.60	-16.1	13.1%	-0.47	-2.12	truncated curve
UGC 8919N	—	—	—	—	-2.69	truncated curve
CGCG 132-062	1.00	-16.9	14.9%	-1.63	-3.44	truncated curve

Note. — Origins of the TF Outliers: (1) Name, (2) burst strength in R , or the fraction of R flux in the slit of the BGK spectroscopic aperture that originates from the new burst (computed with the technique of Fig. 15), (3) R magnitude of this central star formation in the spectroscopic aperture, (4) fraction of the total R flux of the galaxy that is in the spectroscopic aperture, (5) expected TF shift from the new flux in the central aperture (assuming an initial luminosity appropriate for its η and the C97 TF relation), (6) actual residual from the C97 TF relation, (7) our best guess as to the primary physical origin of the TF residual (see Secs. 4.2 – 4.4). Two galaxies (UGC 4774 and UGC 8919N) are outside the contour boundaries of Fig. 15; we have no burst strength solutions for these galaxies.

Table 7. Pair TF Residuals vs. Continuous Third Parameters, Spearman Rank Correlation Tests

Test	Measure	C97 (-6.36)	Spearman Rank Probabilities			
			unbiased (-5.58)	least-squares (-4.75)	η $\log(\text{km/s})$	M_R (mag.)
Kinematic distortion	χ_{rc}^2	0.101	0.177	0.360	0.017	0.084
Curve truncation	$R_{\text{max}}/R_{\text{disk}}$	0.273	0.662	0.995	0.170	0.241
Tidal stretching	$R_{\text{disk}} (\text{h}^{-1} \text{kpc})$	0.233	0.010	2.26×10^{-5}	2.02×10^{-10}	4.28×10^{-18}
Morphological distortion	χ_{phot}^2	0.672	0.891	0.956	0.466	0.632
Star formation	$\text{EW}(\text{H}\alpha)$ ^a	0.274	0.783	0.407	6.80×10^{-6}	3.89×10^{-6}
Star formation	$B - R$, galaxy	0.023	0.198	0.998	8.24×10^{-9}	6.36×10^{-7}
Star formation	$B - R$, center ^a	0.683	0.709	0.152	1.86×10^{-5}	3.63×10^{-6}
Burst strength	s_R ^b	0.500	0.248	0.149	0.055	6.82×10^{-3}
TF parameters	η	3.14×10^{-4}	0.049	0.95		
	M_R	0.425	0.016	5.57×10^{-6}		

^aIncludes only the 89 galaxies with separate nuclear spectra.

^bIncludes only the 48 galaxies with valid solutions.

Note. — Spearman rank probabilities of no correlation with third parameters: (1) quantity that parameter tests, (2) parameter (see Sec. 5.2), (3) – (5) P_{SR} of no correlations with the TF residuals, assuming the C97 slope, -6.36, the slope from the Willick (1994) technique, -5.58, and the straight linear least-squares slope for the pairs (with no outliers), -4.75 respectively, and (6) – (7) P_{SR} of no correlations with the TF parameters, η and M_R .

Table 8. TF Residual – Discrete Third Parameter Kolmogorov-Smirnov Tests

Test	Measure	N ₁	N ₂	Kolmogorov-Smirnov Probabilities				η log(km/s)	M _R (mag.)
				C97 (-6.36)	unbiased (-5.58)	least-squares (-4.75)			
Kinematic distortion	“Normal” vs. “Marginal”	39	34	0.810	0.681	0.934	0.110	0.229	
	“Normal” vs. “Distorted”	39	9	0.003	0.005	0.003	0.848	0.100	
	“Normal” vs. “Distorted”	31	39	0.359	0.259	0.085	0.953	0.125	
	well-determined ϵ vs. poor, no-fit	60	22	0.774	0.659	0.606	0.185	0.069	
Overlap	unobstructed vs. overlapping galaxies	37	31	0.863	0.908	0.548	0.201	0.246	
	unobstructed vs. overlapping star(s)	37	12	0.916	0.804	0.901	0.489	0.375	

Note. — Kolmogorov-Smirnov probabilities for the distributions of TF residuals for subsamples separated based on discrete third parameters: (1) quantity that parameter measures, (2) distributions compared, (3) number of galaxies in first set, (4) number of galaxies in second set, (5) – (7) P_{KS} for the distributions of TF residuals, measured assuming the C97 slope, -6.36, the slope from the Willick (1994) technique, -5.58, and the straight linear least-squares slope for the pairs (with no outliers), -4.75 respectively, and (8) – (9) P_{KS} for the distributions of η and M_R.

Table 9. Outlier Parameters

Parameter	UGC 4744	UGC 312E	NGC 7253B	UGC 6944	UGC 7085W	NGC 2719A	UGC 8919N	CGCG 132-062
χ^2_{rc}	2.9	7.1	11.2	12.4	5.5	1.4	3.0	3.0
$R_{\text{max}}/R_{\text{disk}}$	0.3	5.2	3.5	4.5	1.8	2.9	0.2	1.4
R_{disk} (h $^{-1}$ kpc)	8.2	2.4	1.8	2.2	1.8	1.0	3.6	0.9
χ^2_{phot}	0.2	18.1	81.1	1.5	0.2	0.2	0.1	1.8
EW(H α)	0.0	71.0	15.4	79.3	21.4	100.2	7.1	62.0
$B - R$, galaxy	1.4	0.6	1.0	0.6	0.7	0.4	1.1	1.0
$B - R$, center	1.2	0.4	0.9	0.2	0.7	0.7	0.6	-0.1
s_R	–	0.8	0.4	1.0	0.6	0.6	–	1.0
Rotation curve ^a	N	D	D	D	D	M	M	M
Morphology ^b	D	D	D	D	N	N	N	N
ϵ measurement ^c	F	P	P	W	W	F	W	P
Overlapping? ^d	S/G	N	G	S	S	G	G	S

^aN=normal, M=marginal, D=distorted

^bN=normal, U=unknown, D=distorted

^cW=well-determined, P=poor fit, F=not fit

^dN=normal, S=star(s) overlapping, G=galaxies overlap

Note. — “Third parameter” values for the 8 outliers. See the parameter descriptions in Sec. 5.1.